

Unimon qubit

Received: 4 May 2022

Accepted: 28 October 2022

Published online: 12 November 2022

 Check for updates

Eric Hyyppä¹✉, Suman Kundu², Chun Fai Chan¹, András Gunyhó², Juho Hotari¹, David Janzso¹, Kristinn Juliusson¹, Olavi Kiuru², Janne Kotilahti¹, Alessandro Landra¹, Wei Liu¹, Fabian Marxer¹, Akseli Mäkinen¹, Jean-Luc Orgiazzi¹, Mario Palma¹, Mykhailo Savytskyi¹, Francesca Tosto¹, Jani Tuorila¹, Vasilii Vadimov², Tianyi Li¹, Caspar Ockeloen-Korppi¹, Johannes Heinsoo^{1,4}, Kuan Yen Tan^{1,4}, Juha Hassel^{1,4} & Mikko Möttönen^{1,2,3,4}✉

Superconducting qubits seem promising for useful quantum computers, but the currently wide-spread qubit designs and techniques do not yet provide high enough performance. Here, we introduce a superconducting-qubit type, the *unimon*, which combines the desired properties of increased anharmonicity, full insensitivity to dc charge noise, reduced sensitivity to flux noise, and a simple structure consisting only of a single Josephson junction in a resonator. In agreement with our quantum models, we measure the qubit frequency, $\omega_{01}/(2\pi)$, and increased anharmonicity $\alpha/(2\pi)$ at the optimal operation point, yielding, for example, 99.9% and 99.8% fidelity for 13 ns single-qubit gates on two qubits with $(\omega_{01}, \alpha) = (4.49 \text{ GHz}, 434 \text{ MHz}) \times 2\pi$ and $(3.55 \text{ GHz}, 744 \text{ MHz}) \times 2\pi$, respectively. The energy relaxation seems to be dominated by dielectric losses. Thus, improvements of the design, materials, and gate time may promote the unimon to break the 99.99% fidelity target for efficient quantum error correction and possible useful quantum advantage with noisy systems.

Even though quantum supremacy has already been reached with superconducting qubits in specific computational tasks^{1,2}, the current quantum computers still suffer from errors owing to noise to the extent that their practical applications in areas such as physics simulations³, optimization⁴, machine learning⁵, and chemistry⁶ remain out of reach. In this so-called noisy intermediate-scale quantum (NISQ) era⁷, the complexity of the implementable quantum computations⁸ is mostly limited by errors in single- and two-qubit quantum gates. Crudely speaking, the process fidelity of implementing a d -deep n -qubit logic circuit with gate fidelity F is F^{dn} . Thus, to succeed roughly half of the time in a 100-qubit circuit of depth five, one needs at least 99.9% gate fidelity. In practice, the number of qubits and especially the gate depth required for useful NISQ advantage is likely higher, leading to a fidelity target of 99.99% for all quantum gates, not yet demonstrated in any superconducting quantum computer.

The effect of gate errors can be reduced to some extent using error mitigation^{9,10} or in principle, completely using quantum error

correction¹¹. Surface codes^{12,13} are regarded as some of the most compelling error correction codes for superconducting qubits owing to the two-dimensional topology of the qubit register and their favorable fidelity threshold of roughly 99% which has been reached with superconducting transmon qubits already in 2014¹⁴ with following important steps reported in refs. 15, 16. Despite the recent major developments in implementing distance-2–5 surface codes on superconducting quantum processors^{17–23}, the gate and readout fidelities of superconducting qubits need to be improved further, preferably above 99.99%, to enable efficient quantum error correction with a reasonable qubit count.

Currently, most of the superconducting multi-qubit processors utilize transmon qubits^{1,17,24,25} that can be reproducibly fabricated²⁴ and have coherence times up to several hundred microseconds^{26,27}, leading to record average gate fidelities of 99.98–99.99% for single-qubit gates^{28,29} and 99.8–99.9% for two-qubit gates^{30,31}. The transmon was derived from the charge qubit³² by adding a shunt capacitor in parallel

¹IQM, Keilaranta 19, 02150 Espoo, Finland. ²QCD Labs, QTF Centre of Excellence, Department of Applied Physics, Aalto University, P.O. Box 13500, FIN-00076 Aalto, Finland. ³VTT Technical Research Centre of Finland Ltd. & QTF Centre of Excellence, P.O. Box 1000, 02044 VTT Espoo, Finland. ⁴These authors jointly supervised this work: Johannes Heinsoo, Kuan Yen Tan, Juha Hassel, Mikko Möttönen. ✉ e-mail: eric@meetiqm.com; mikko.mottonen@aalto.fi

with a Josephson junction, with the result of exponentially suppressing the susceptibility of its transition frequency to charge noise. However, the large shunt capacitance results in a relatively low anharmonicity of 200–300 MHz corresponding to only 5% of the typical qubit frequency^{33,34}. This limits the speed of quantum gates that can be implemented with transmons since leakage errors to the states beyond the computational subspace need to be suppressed^{28,35}. Similarly, the low anharmonicity also limits the readout speed of transmon qubits and a high-power readout tone can even excite the transmon to unconfined states beyond the cosine potential³⁶ (see Supplementary Note II in Supplementary Materials). A higher anharmonicity is preferred to speed up the qubit operations and to allow for higher fidelities limited by the finite coherence time.

Hence, it is desirable to find new superconducting qubit types that increase the anharmonicity–coherence-time product. Recently, major progress has been made in the development of fluxonium qubits, one of the most compelling alternatives to transmons thanks to their high anharmonicity and long relaxation and coherence times^{37–39} which recently enabled an average gate fidelity exceeding 99.99% for single-qubit gates⁴⁰ and 99.7% for a two-qubit gate³⁸. In a fluxonium qubit, a small Josephson junction is shunted by a superinductor implemented by an array of large Josephson junctions^{37,39,41}, a granular aluminum wire⁴², a nanowire with a high kinetic inductance⁴³, or a geometric superinductor⁴⁴. The superinductor in the fluxonium ensures that the dephasing and relaxation rates arising from flux noise are reduced, in addition to which all the levels of a fluxonium are fully protected against dephasing arising from low-frequency charge noise. It is possible to add a large shunt capacitor into the fluxonium in order to create a so-called heavy fluxonium^{39,45}, in which the transition matrix element between the ground state and the first excited state can be suppressed to enhance the relaxation time up to the millisecond regime⁴⁵. However, special techniques are required to control, readout, and reset these high-coherence fluxonium qubits due to their low frequency and small transition matrix elements in the vicinity of the half flux quantum operation point³⁹. Furthermore, these qubits do not achieve protection against both relaxation and dephasing due to flux noise at a single operation point. Parasitic capacitances in the superinductor may also provide a challenge for the reproducible fabrication of fluxonium qubits and result in parasitic modes.

By reducing the total inductance of the junction array in the fluxonium, it is possible to implement a plasmonium qubit⁴⁶ operated at zero flux or a quarton qubit⁴⁷ operated at the half-flux-quantum point, both of which have a small size and a high anharmonicity compared with the transmon and a sufficient protection against charge noise in comparison to current coherence times. On the other hand, an enhancement of the superinductance converts the fluxonium into a so-called quasicharge qubit⁴⁸, the charge-basis eigenstates of which resemble those of the early charge qubits while retaining the protection against charge noise. Other qubits protected against some sources of relaxation and dephasing include the $0-\pi$ qubit⁴⁹, bifluxon⁵⁰, and a qubit protected by two-Cooper-pair tunneling⁵¹. The $0-\pi$ qubit is protected against both relaxation and dephasing arising from charge and flux noise thanks to its topological features, which unfortunately renders the qubit challenging to operate and its circuit relatively complicated and hence vulnerable to parasitic capacitance. Despite this great progress in fluxonium and protected qubits, they have still not shown broad superiority to the transmons. The race for the new improved mainstream superconducting qubit continues.

In this work, we introduce and demonstrate a novel superconducting qubit, *the unimon*, that consists of a single Josephson junction shunted by a linear inductor and a capacitor in a largely unexplored parameter regime where the inductive energy is mostly cancelled by the Josephson energy leading to high anharmonicity while being fully resilient against low-frequency charge noise and partially protected from flux noise (Fig. 1). We measure the unimon frequency

and anharmonicity in a broad range of flux biases and find a very good agreement with first-principles models (Fig. 2), even for five different qubits (Fig. 3a). According to our experimental data, the energy relaxation time seems to be limited by dielectric losses (Fig. 3b), and the coherence time can be protected from flux noise at a flux-insensitive sweet spot (Fig. 3c). Importantly, we observe that the single-qubit gate fidelity progressively increases with decreasing gate duration, and is stable for hours at 99.9% for a 13 ns gate duration (Fig. 4).

Results

Unimon qubit

In practice, we implement the unimon in a simple superconducting circuit by integrating a single Josephson junction into the center conductor of a superconducting coplanar-waveguide (CPW) resonator grounded at both ends (Fig. 1b). There are no charge islands in the circuit, and hence the junction is inductively shunted. In addition to the very recent fluxonium qubit utilizing a geometric superinductance⁴⁴, the unimon is the only superconducting qubit with the Josephson junction shunted by a geometric inductance that provides complete protection against low-frequency charge noise. Due to the non-linearity of the Josephson junction, the normal modes of the resonator with a non-zero current across the junction are converted into anharmonic oscillators that can be used as qubits. In this work, we use the lowest anharmonic mode as the qubit since it has the highest anharmonicity.

The frequency of each anharmonic mode can be controlled by applying external fluxes $\Phi_{\text{ext},1}$ and $\Phi_{\text{ext},2}$ through the two superconducting loops of the resonator structure as illustrated in Fig. 1b. The unimon is partially protected against flux noise thanks to its gradiometric structure, which signifies that the superconducting phase across the Josephson junction is dependent on the half difference of the applied external magnetic fluxes $\Phi_{\text{diff}} = (\Phi_{\text{ext},2} - \Phi_{\text{ext},1})/2$. Interestingly, the anharmonicity of the unimon is maximized at a flux-insensitive sweet spot, at which the qubit frequency is unaffected by the external flux difference to the first order. This optimal operation point is obtained at $\Phi_{\text{diff}} = \Phi_0/2$ modulo integer flux quanta $\Phi_0 = h/(2e) \approx 2.067 \times 10^{-15}$ Wb, where h is the Planck constant and e is the elementary charge.

Using the distributed-element circuit model shown in Fig. 1c, the effective Hamiltonian of the qubit mode m can be written (model I in “Methods”) as

$$\hat{H}_m = 4E_{C,m}(\varphi_0)\hat{n}_m^2 + \frac{1}{2}E_{L,m}(\varphi_0)\hat{\varphi}_m^2 + E_L\hat{\varphi}_m \left(\frac{2\pi\Phi_{\text{diff}}}{\Phi_0} - \varphi_0 \right) - E_J \cos(\hat{\varphi}_m - \varphi_0), \quad (1)$$

where φ_0 is the Josephson phase of a dc current across the junction, $E_{C,m}(\varphi_0)$ is the capacitive energy of the qubit mode, $E_{L,m}(\varphi_0)$ is the inductive energy of the qubit mode, E_L is the inductive energy of the dc current, E_J is the Josephson energy, and \hat{n}_m and $\hat{\varphi}_m$ are the Cooper pair number and phase operators corresponding to the qubit mode m and satisfying $[\hat{\varphi}_m, \hat{n}_m] = i$ with i being the imaginary unit. Note that φ_0 is treated as a classical variable depending on the flux bias Φ_{diff} according to a transcendental equation such that $2\pi\Phi_{\text{diff}}/\Phi_0 - \varphi_0$ is periodic in Φ_{diff} . (See Fig. 5 for solutions of Eq. (1).)

At the sweet spot $\Phi_{\text{diff}} = \Phi_0/2$, the dc phase equals $\varphi_0 = \pi$ and the Hamiltonian of the unimon reduces to

$$\hat{H}_m = 4E_{C,m}(\pi)\hat{n}_m^2 + \frac{1}{2}E_{L,m}(\pi)\hat{\varphi}_m^2 + E_J \cos(\hat{\varphi}_m), \quad (2)$$

where we assume that $E_J \leq E_L$. Strikingly, this Hamiltonian is exactly analogous to a simple mechanical system visualized in Fig. 1d, in which an inverted pendulum is attached to a twisting beam. In this analogy,

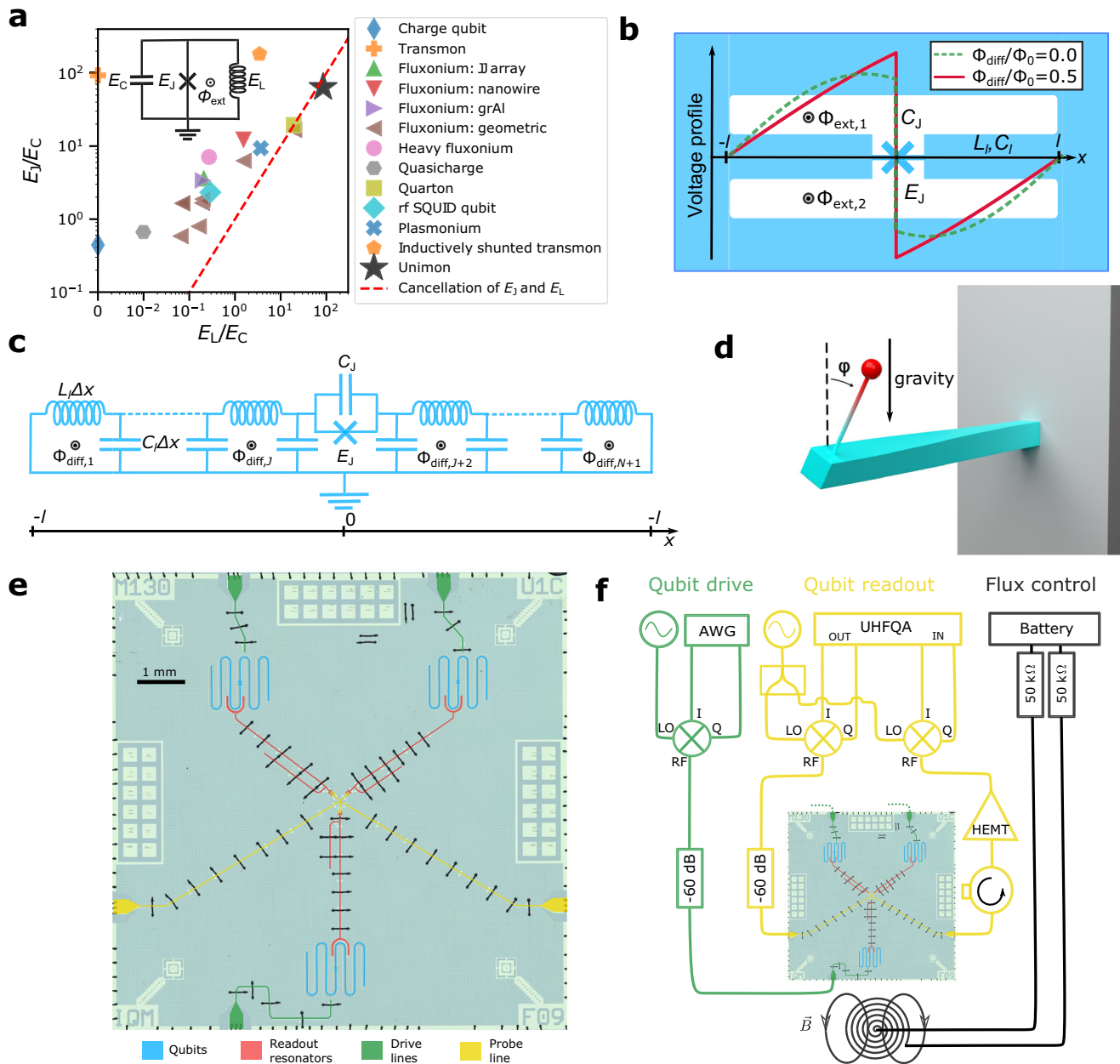


Fig. 1 | Unimon qubit and its measurement setup. **a** Superconducting-qubit types, described by the circuit in the inset, mapped by their energy scales: Josephson energy E_J and inductive energy E_L compared with the charging energy E_C . Unimons lie near the red dashed line leading to the cancellation of the linear inductive energy by the quadratic contribution of the Josephson energy at half flux quantum $\Phi_0/2$. The black star denotes the unimons realized in this work and the other experimental data points are from refs. 32, 34, 37, 39, 42–44, 46–48, 80, 81. **b** Schematic unimon circuit consisting of a Josephson junction (E_J, C_J) in a grounded coplanar-waveguide (CPW) resonator of length $2l$ and an inductance and capacitance per unit length of L_l and C_l , respectively. The voltage envelope functions of the qubit mode are also illustrated at external-flux biases $\Phi_{\text{diff}} = (\Phi_{\text{ext},2} - \Phi_{\text{ext},1})/2 = 0.0$ (dashed line) and $\Phi_{\text{diff}} = \Phi_0/2$ (solid line). **c** Distributed-element circuit

model of the unimon, in which the CPW is modeled by N inductors $L_l \Delta x$ and capacitors $C_l \Delta x$, where $\Delta x = 2l/N$. **d** Schematic illustration of a mechanical inverted pendulum system, the Hamiltonian of which is identical to that of the lumped-element unimon circuit in (a). In this analogy, the gravitational potential energy corresponds to the Josephson potential, the harmonic potential energy of the twisting beam corresponds to the inductive energy, the moment of inertia corresponds to the capacitance of the unimon, and the angle of the zero twist position corresponds to the flux bias Φ_{diff} . **e** False-color microscope image of a silicon chip containing three unimon qubits (blue) together with their readout resonators (red), drive lines (green), and a joint probe line (yellow). **f** Simplified experimental setup used to measure the unimon qubits at 10 mK (see Supplementary Methods IV for details).

the gravitational potential energy of the pendulum corresponds to the cosine-shaped Josephson potential, the harmonic potential energy associated with the twisting of the beam corresponds to the inductive energy of the unimon, and the moment of inertia of the pendulum is analogous to the capacitance in the unimon. Furthermore, the twist angle φ is analogous to the superconducting phase difference $\hat{\varphi}_m$ of the qubit mode across the Josephson junction. This mechanical analog provides great intuition to the physics of the unimon.

In this work, we employ the parameter regime $E_J \lesssim E_{L,m}(\pi) \approx E_L$ to provide a large anharmonicity without any superinductors. As a result, it is instructive to use the Taylor expansion of the cosine and write the sweet-spot Hamiltonian of the unimon in Eq. (2) as

$$\hat{H}_m = 4E_{C,m}(\pi)\hat{n}_m^2 + \frac{E_{L,m}(\pi) - E_J}{2}\hat{\varphi}_m^2 + \frac{E_J}{24}\hat{\varphi}_m^4 + \mathcal{O}(\hat{\varphi}_m^6). \quad (3)$$

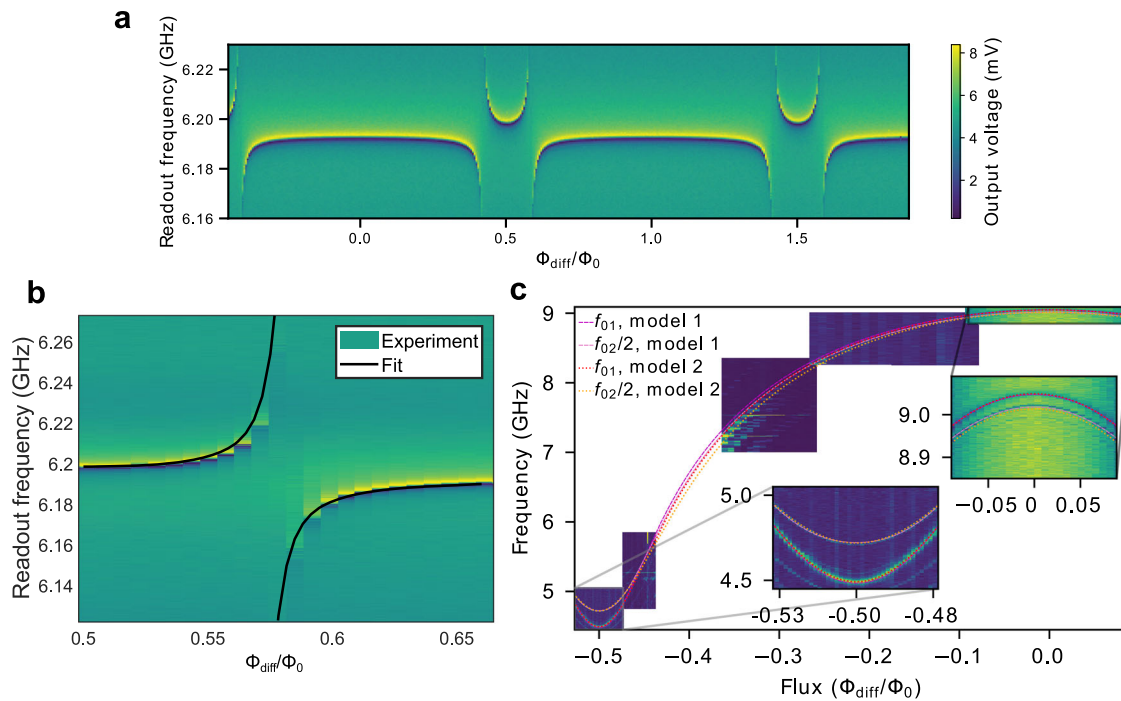


Fig. 2 | Resonator and qubit B spectroscopies. **a** Magnitude of the readout signal voltage transmitted through the probe line as a function of the signal frequency and the flux bias Φ_{diff} of the unimon. **b** Magnification at an avoided crossings of **a**, where a unimon and its readout resonator are close to resonance, together with a fit (solid black line) used to estimate the coupling capacitance C_g between the qubit and the resonator. The fit is based on diagonalizing Eq (5) in “Methods”. **c** Magnitude of the

readout signal at a properly chosen readout frequency as a function of the flux bias Φ_{diff} and qubit excitation frequency, revealing the spectral lines of the unimon together with global fits to the theoretical model 1 and 2 (“Methods”). The insets show magnifications at the flux sweet spots, highlighting that at half flux quantum, the unimon frequency is minimized whereas its anharmonicity is maximized.

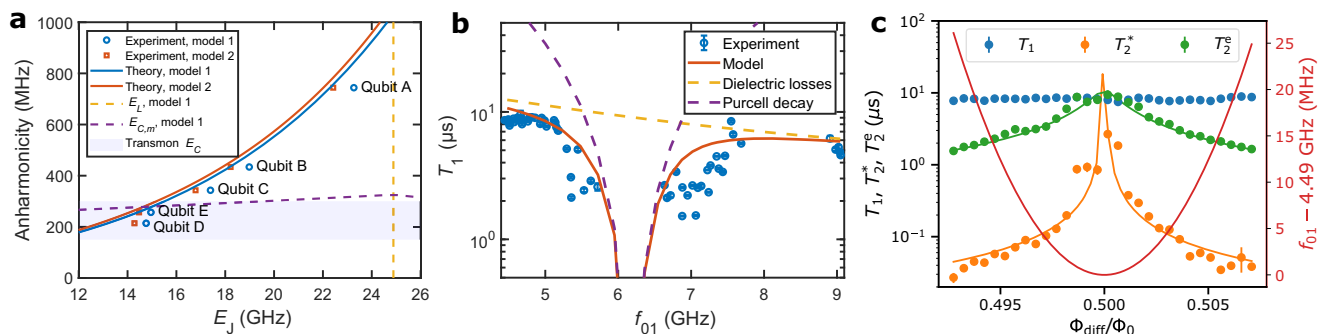


Fig. 3 | Measurement of key qubit properties. **a** Predicted (solid lines) and measured anharmonicities of five unimon qubits (markers) at flux bias $\Phi_{\text{diff}} = \Phi_0/2$ as functions of the Josephson energy E_J estimated from data similar to Fig. 2c using the models 1 (blue color) and 2 (orange color) presented in “Methods”. The dashed yellow line highlights the E_J that perfectly cancels the linear inductive energy in model 1. The capacitive qubit energy $E_{C,m}$ in model 1 follows the dashed purple line, whereas the purple shading visualizes typical transmon anharmonicities. **b** Experimentally measured mean energy relaxation time T_1 of qubit B (blue circles) as a function of the qubit frequency f_{01} together with a model (solid line) taking into account dielectric losses (dashed yellow line) and the Purcell decay (dashed purple

line). The error bars represent the standard error of the mean obtained from 6 to 30 repetitions of single T_1 measurements conducted at each frequency. **c** Relaxation time T_1 , Ramsey coherence time T_2^* , and echo coherence time T_2^c of qubit B as functions of the flux bias Φ_{diff} in the vicinity of $\Phi_{\text{diff}} = \Phi_0/2$. The error bars of T_1 and T_2^* represent the standard error of the mean based on 8 repeated experiments, whereas the error bars of T_2^c represent the standard error derived from the standard deviations of the fitted dephasing rates $\Gamma_{\phi,\phi}^c$ and $\Gamma_{\phi,0}^c$ by applying Eq. (12). The green and orange lines illustrate fits to T_2^* and T_2^c data based on models regarding the dephasing rate as a linear function of $\partial f_{01}/\partial \Phi_{\text{diff}}$ (“Methods”). The red line shows the detuning of the qubit frequency from its minimum value 4.49 GHz.

The quadratic term proportional to $(E_{L,m}(\pi) - E_J)$ is mostly cancelled in the unimon regime, which emphasizes the high-order terms in the potential energy and hence increases the anharmonicity of the qubit. This cancellation bears resemblance to the quarton qubit⁴⁷ with the distinctive difference that the quadratic inductive energy of a quarton qubit is only an approximation for the actual potential energy function of a short Josephson junction array, as a result of which the quarton circuit is not fully protected against low-frequency charge noise unlike the unimon.

To experimentally demonstrate the unimon qubit, we design and fabricate samples, each of which consists of three unimon qubits as illustrated in Fig. 1e. We use niobium as the superconducting material apart from the Josephson junctions, in which the superconducting leads are fabricated using aluminum (see Sample Fabrication in Methods). The CPW structure of the unimon is designed for characteristic impedance $Z = 100 \Omega$ to reduce the total capacitance of the unimon in comparison to a standard 50Ω resonator. Each qubit is capacitively coupled to an individual drive line that enables single-

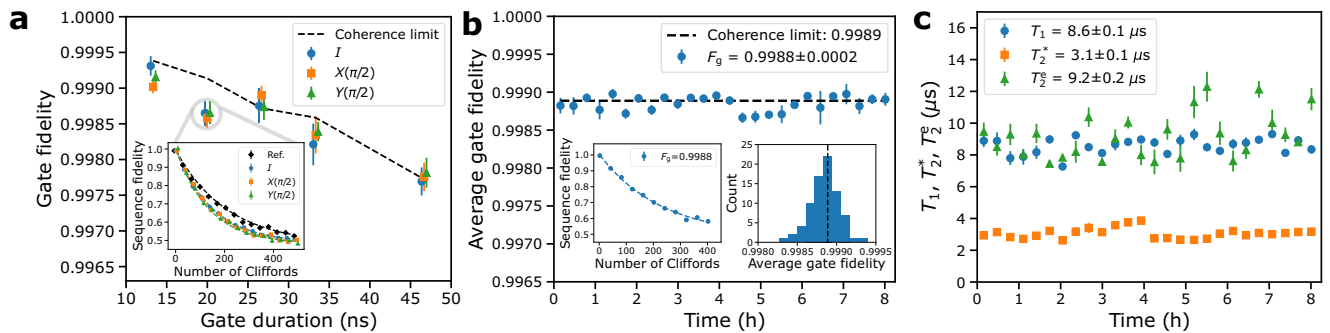


Fig. 4 | Implementation of fast and stable single-qubit gates for qubit B. **a** Average gate fidelity as a function of the gate duration for gates in the set $\{I, X(\pi/2), Y(\pi/2)\}$. The error bars represent the standard error of the mean based on six interleaved randomized benchmarking experiments. The dashed black line shows the coherence limit computed based on the mean values of the energy relaxation time T_1 and the echo coherence time T_2^* . The inset shows the results of an exemplary interleaved randomized benchmarking experiment corresponding to a gate duration of 20 ns. **b** Average gate fidelity F_g measured with randomized benchmarking as a function of time lapsed from the initial gate and parameter calibration. The error bars represent the standard error of the

mean from three consecutive randomized benchmarking experiments. The dashed black line shows the coherence limit that has been computed using the mean values of T_1 and T_2^* measured interleaved with the gate fidelity. The left inset illustrates the decay of the sequence fidelity as a function of its length in an exemplary randomized-benchmarking experiment. The right inset shows the histogram of the gate fidelities obtained over the measurement period of eight hours. **c** Stability of T_1 , T_2^* , and the Ramsey coherence time T_2^* over a period of eight hours. The qubit parameters were calibrated only once before the characterization measurements. The error bars represent the standard error of the mean from three consecutive measurements.

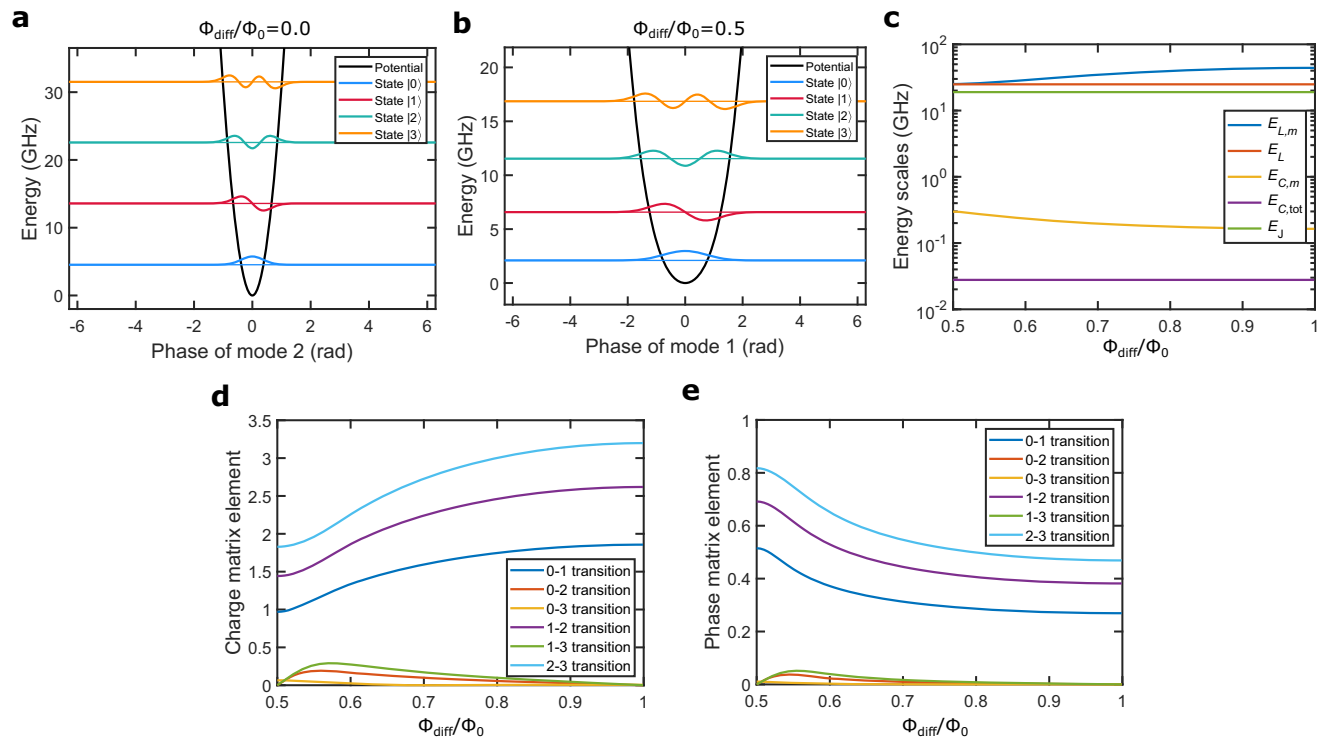


Fig. 5 | Potential-energy function, energy scales, and matrix elements of qubit B based on model 1. **a, b** Potential energy of the unimon based on equation (4) in Methods as a function of the phase variable φ_m of mode m together with the four lowest eigenenergies and corresponding phase-basis wave functions at flux biases of $\Phi_{\text{diff}} = 0$ (**a**) and $\Phi_{\text{diff}} = \Phi_0/2$ (**b**). Note that the second mode of the circuit is used as the qubit at $\Phi_{\text{diff}} = 0$ and the first mode at $\Phi_{\text{diff}} = \Phi_0/2$. **c** Energy scales $E_{C,m}$, $E_{L,m}$, E_L , and E_J of the qubit as functions of Φ_{diff} . Here, $E_{C,m}$ and $E_{L,m}$ are the capacitive and inductive energies of the qubit mode, E_L is the inductive energy corresponding to a

dc current in the center conductor of the qubit, and E_J is the Josephson energy. We also show an effective charging energy $E_{C,\text{tot}} = e^2/(4C_l)$ computed based on the total capacitance $2C_l$ of the transmission line of the unimon. **d** Off-diagonal matrix elements $|\langle i|\hat{n}_m|j\rangle|$ of the Cooper pair number operator \hat{n}_m for the four lowest-energy states of the qubit mode m as functions of Φ_{diff} . **e**, As **d** but for the phase operator $\hat{\varphi}_m$. In all panels, the results have been obtained by using the theoretical model 1 in “Methods” and the measured parameter values of qubit B reported in Table 1.

qubit rotations in a similar manner as for conventional transmon qubits by applying attenuated microwave pulses along the drive line as illustrated in the simplified schematic of the experimental setup in Fig. 1f (see also Supplementary Methods IV for a more detailed illustration of the setup). All experiments are carried out at 10 mK base temperature of a pulse-tube-cooled dilution refrigerator. Furthermore,

each qubit is capacitively coupled to a readout resonator using a U-shaped capacitor in order to enable dispersive qubit state measurements^{52,53} similar to those conventionally used with transmon qubits²⁰. The frequency of the qubits is tuned by applying a current through an external coil attached to the sample holder such that one flux quantum Φ_0 approximately corresponds to 10 μ A.

Table 1 | Characteristic parameter values for the five measured unimon qubits

Qubit	2l (mm)	L _l (μH/m)	C _l (pF/m)	E _J /h (GHz)	E _{L,m} /h (GHz)	E _{C,m} /h (GHz)	ω ₀₁ /(2π) (GHz)	α/(2π) (MHz)	x _g (mm)	C _g (fF)	g ₀₁ /(2π) (MHz)	χ/(2π) (MHz)	f _r (GHz)	κ/(2π) (MHz)
A	8.0	0.821*	87.1*	23.3	24.9	0.318	3.547	744	0.596	9	53.5	0.74	5.826	0.43
B	8.0	0.821	87.1	19.0	25.2	0.297	4.488	434	0.596	10	70.0	1.2	6.198	1.24
C	8.0	0.821*	87.1*	17.4	25.3	0.290	4.781	343	0.596	12.5	79.7	9.20	5.522	9.2
D	8.0	0.821*	87.1*	14.8	25.7	0.278	5.257	214	0.596	12.5	85.7	20.2	5.699	10.0
E	8.0	0.821*	87.1*	15.0	25.7	0.279	5.224	257	0.596	12.5	92.3	4.1	6.156	1.8

For each of the characterized qubits, the data includes the total length 2l of the center conductor in the qubit, the fitted inductance L_l and capacitance C_l per unit length of the center conductor, the fitted Josephson energy E_J, the inductive and capacitive energies E_{L,m} and E_{C,m}, the measured qubit frequency ω₀₁/(2π), the measured anharmonicity α/(2π), the location x_g of the unimon–resonator coupling point with respect to the junction, the measured coupling strength |g₀₁|/(2π) between the qubit and its readout resonator providing the corresponding coupling capacitance C_g, the measured dispersive shift χ/(2π), the measured frequency of the readout resonator f_r, and the measured linewidth of the readout resonator κ/(2π). All the fitted values were estimated using theory model 1 (“Methods”). The values of the flux-dependent quantities E_{L,m}, E_{C,m}, ω₀₁/(2π), α/(2π), g₀₁/(2π), χ/(2π), and f_r are reported at Φ_{diff} = Φ₀/2. The asterisks denote the fact that the inductance L_l and capacitance C_l per unit length are estimated by fitting the theoretical model to the spectrum of qubit B and that equal values are used for the other qubits due to an identical cross section of the co-planar waveguide in all qubits. The inductive and capacitive energies E_{L,m} and E_{C,m} are computed using the theoretical model 1 (“Methods”) which is also used to obtain the measured values of E_J, L_l, and C_l.

Table 2 | Results of coherence characterization and randomized-benchmarking (RB) experiments for the five unimon qubits

Qubit	Φ _{diff} = Φ ₀ /2					Gate duration (ns)
	T ₁ (μs)	T ₂ [*] (μs)	T ₂ ^e (μs)	A _{Φ_{diff}} (μΦ ₀)	RB fidelity (%)	
A	7.2	1.9	6.8	6.1	99.81	13.3
B	8.6	3.1	9.2	15.0	99.90	13.3
C	5.8	2.3	9.3	11.2	99.54	40
D	3.9	2.3	7.0	11.1	99.63	20
E	5.6	2.5	11.4	14.3	99.86	13.3

The measured energy relaxation time T₁, the measured Ramsey coherence time T₂^{*}, the measured echo coherence time T₂^e, the flux noise density parameter A_{Φ_{diff}} at 1 Hz estimated from the echo coherence time, the average fidelity per microwave gate from standard RB experiments, and the gate duration used in the RB experiments. All of the values are measured in the immediate vicinity of the sweet spot Φ_{diff} = Φ₀/2.

Experimental results on unimons

We experimentally study five unimon qubits, A–E, on two different chips. In all of the qubits, the geometry of the CPW resonator is similar, but the qubits have different Josephson energies E_J corresponding to different amounts of cancellation ∝ (E_{L,m}(π) – E_J) of the quadratic potential energy terms. Furthermore, the coupling capacitance between a qubit and its readout resonator has been designed to be different on the two chips. We present the main measured properties for all of the five qubits in Tables 1 and 2. Design targets of the parameter values are provided in Supplementary Table 2 in Supplementary Methods V. The results discussed below are obtained from qubit B unless otherwise stated.

In Fig. 2a, we show the microwave response of the readout resonator as a function of the flux bias Φ_{diff} through the unimon loops. We observe that the frequency of the readout resonator changes periodically, as expected, since a change of flux by a flux quantum has no observable effect on the full circuit Hamiltonian in Eq. (1). Furthermore, the frequency of the readout resonator exhibits an avoided crossing where the first transition frequency of the bare qubit f₀₁ = ω₀₁/(2π) crosses the bare resonator frequency. By fitting our theoretical model of the coupled unimon–resonator system (see Methods and Supplementary Methods II) to the experimental data of the avoided crossing shown in Fig. 2b, we estimate that the coupling capacitance between the qubit and the readout resonator is C_g = 10.0 fF in good agreement with the design value of 10.4 fF obtained from our classical electromagnetic simulations.

Figure 2c shows the results of a two-tone experiment to map the qubit frequency spectrum (Methods). We observe that the single-

photon transition between the ground state |0⟩ and the first excited state |1⟩ has a minimum frequency of f₀₁ = 4.488 GHz at Φ_{diff}/Φ₀ = –0.5 and a maximum frequency of f₀₁ = 9.05 GHz at Φ_{diff} = 0. The two-photon transition |0⟩ ↔ |2⟩ is also clearly visible, which allows us to verify that the anharmonicity α/(2π) = f₁₂ – f₀₁ of the qubit is enhanced at the sweet spot Φ_{diff}/Φ₀ = –0.5 to α/(2π) = 434 MHz. (See Fig. 6 for an alternative agreeing way to measure the anharmonicity.)

Figure 2c presents fits to the experimental transition frequencies f₀₁ and f₀₂/2 based on two theoretical models of the circuit Hamiltonian, the first of which corresponds to Eq. (1) (model 1 in “Methods”) and the second of which is based on a path integral approach that does not require the dc phase φ₀ to be treated as a classical variable (model 2 in Methods). The fits agree very well with the experimental transition frequencies, especially near the sweet spots Φ_{diff} = 0 and Φ_{diff}/Φ₀ = –0.5. Importantly, this good agreement with the models and the qubit frequency and anharmonicity is obtained with only three fitting parameters in a broad range of flux biases, and hence confirms our interpretation of the unimon physics (Fig. 1d) and justifies the use of the models for reliable predictions of promising parameter regimes. According to the fits of model 1 (model 2), the capacitance and inductance per unit length of the unimon have a value of C_l = 87.1 pF/m (C_l = 79.8 pF/m) and L_l = 0.821 μH/m (L_l = 0.893 μH/m), respectively, in good agreement with the design values of C_l = 83 pF/m and L_l = 0.83 μH/m.

The measured sweet-spot anharmonicities of the five qubits are shown in Fig. 3a as functions of the Josephson energy E_J that is estimated by fitting the models 1 and 2 to the qubit spectroscopy data as in Fig. 2c. The measured anharmonicities are slightly lower, but very close to the values predicted by the two theoretical models. The qubits A and B exhibit the highest anharmonicities of α/(2π) = 744 MHz and 434 MHz, respectively, as a result of the largest cancellation between the inductive energy E_{L,m} and the Josephson energy E_J. Importantly, the anharmonicity of the qubits A and B is significantly higher than that of typical transmon qubits, 200–300 MHz³⁴. Furthermore, the measured anharmonicities greatly exceed the capacitive energy E_{C,m} of the qubit mode unlike for transmons.

To study the mechanisms determining the energy relaxation time T₁ of the unimon, we measure T₁ as a function of the qubit frequency as shown in Fig. 3b (see also Figs. 7 and 8). At the Φ_{diff} = Φ₀/2 sweet spot, we find T₁ ≈ 8.6 μs, whereas T₁ ≈ 4.6 μs at Φ_{diff} = 0. Between these flux sweet spots, the relaxation time attains a minimum in a frequency range close to the frequency of the readout resonator f_r = 6.198 GHz. This behavior of T₁ can be reasonably explained by dielectric losses with an effective quality factor of Q_C ≈ 3.5 × 10⁵ and Purcell decay through the readout resonator (see “Methods” and Supplementary Methods III). This suggests the qubit energy relaxation to be dominated by dielectric losses at Φ_{diff} = Φ₀/2. The estimated quality factor of this first unimon qubit is almost an order of magnitude higher than

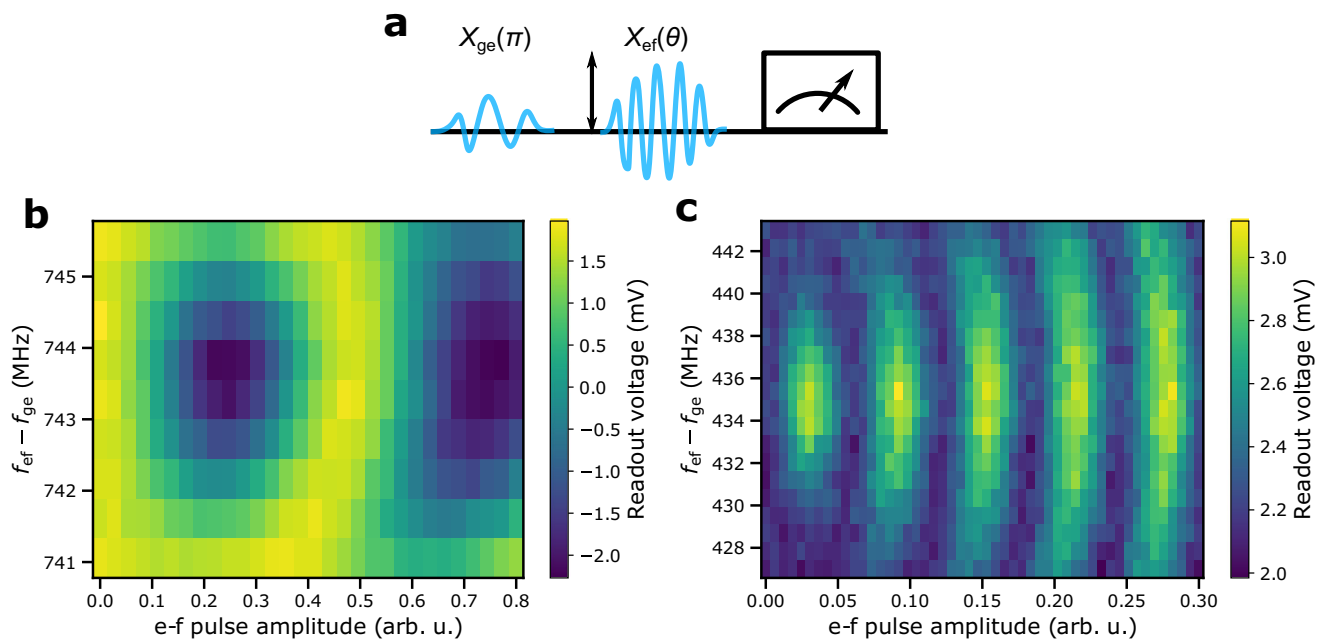


Fig. 6 | Estimation of qubit anharmonicity using Rabi oscillations.

a Measurement sequence of an ef-Rabi experiment. In the experiment, the qubit is first prepared in the excited state with a π -pulse at the frequency f_{ge} matching with the qubit frequency f_{01} followed by another pulse with a fixed duration but a varying frequency f_{ef} and a varying amplitude. After applying the pulses, the output readout voltage is measured. Output readout voltage as a function of the amplitude

of the ef-pulse and the frequency difference $f_{ef} - f_{ge}$ in an ef-Rabi experiment conducted for qubits A (**b**) and B (**c**). The resulting observed Rabi oscillations between the first and the second excited states of the unimon confirm that the anharmonicities α of qubits A and B are approximately 744 MHz and 434 MHz, respectively, as measured using a two-tone qubit spectroscopy such as that shown in Fig. 2c.

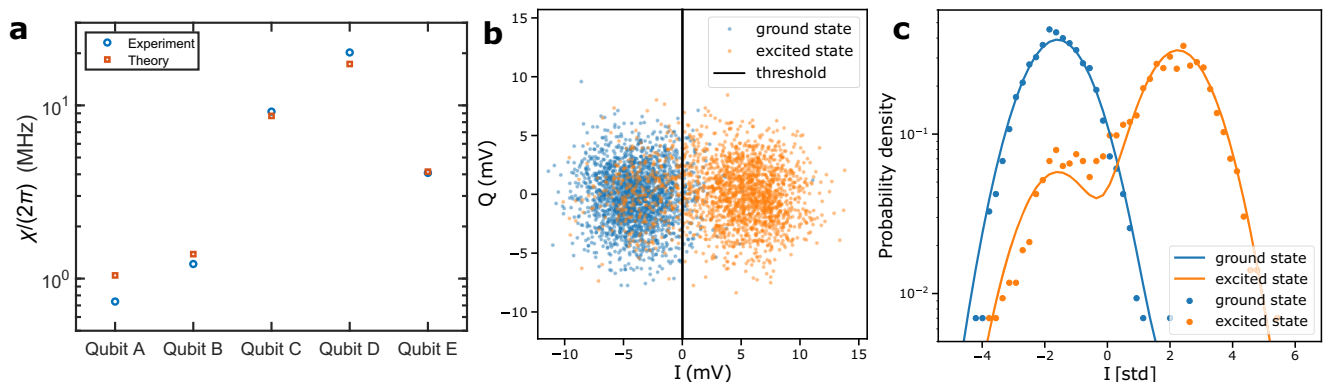


Fig. 7 | Dispersive shift and single-shot qubit readout. **a** Measured dispersive shift χ for different unimon qubits at a flux bias of $\Phi_{\text{diff}} = \Phi_0/2$ (blue circles) together with theoretical predictions (orange squares) computed using Eq. (8) in “Methods” based on the measured qubit frequency, measured anharmonicity, and the fitted coupling capacitance C_g , all of which are reported in Table 1. **b** Readout voltages in the I/Q plane for a single-shot readout experiment conducted for qubit E. The qubit is prepared either to the ground state (blue dots) or to the excited state (orange dots) followed by a single-shot state measurement implemented using a readout pulse with a duration of 1.6 μs . The state preparation was repeated 2000

times for both the ground state and the excited state. The solid black line illustrates the optimal single-shot classification boundary corresponding to a readout fidelity of 89.0%. The classification errors are 5.0 and 17.0% when preparing the qubit to the ground state and to the excited state, respectively. **c** Probability density distributions for the single-shot voltage corresponding to the qubit prepared to the ground state (blue dots) or to the excited state (orange dots). The single-shot voltages have been projected along a line perpendicular to the classification boundary. The solid lines denote fits to the measured probability densities based on a model involving a sum of two Gaussian functions.

for the geometric-superinductance qubits⁵⁴, but of the same order of magnitude as for fluxonium qubits^{39,41} and an order of magnitude lower than in state-of-the-art transmons²⁶. Improvements to design, materials, and fabrication processes are expected to reduce the dielectric losses in future unimon qubits compared with the very first samples presented here.

To characterize the sensitivity of the qubit to flux noise, we measure the Ramsey coherence time T_2^* and the echo coherence time T_2^e with a single echo π -pulse (see Fig. 8) as a function of the flux bias Φ_{diff} . Figure 3c shows that T_2^* and T_2^e are both maximized at $\Phi_{\text{diff}} = \Phi_0/$

2, reaching 3.1 and 9.2 μs , respectively. Away from the sweet spot, the Ramsey coherence time T_2^* degrades quickly, but the echo coherence time T_2^e stays above 1 μs even if the qubit frequency is tuned from the sweet spot by over 30 MHz. Assuming that the flux noise is described by a $1/f$ noise model $S_{\Phi_{\text{diff}}}(\omega) = 2\pi A_{\Phi_{\text{diff}}}^2/\omega$, we estimate a flux noise density of $A_{\Phi_{\text{diff}}}/\sqrt{\text{Hz}} = 15.0 \mu\Phi_0/\sqrt{\text{Hz}}$ based on the flux dependence of T_2^e (“Methods”). The estimated flux noise density is an order of magnitude greater than in state-of-the-art SQUIDS⁵⁵, but an order of magnitude lower than reported for all previous geometric-superinductance qubits⁴⁴.

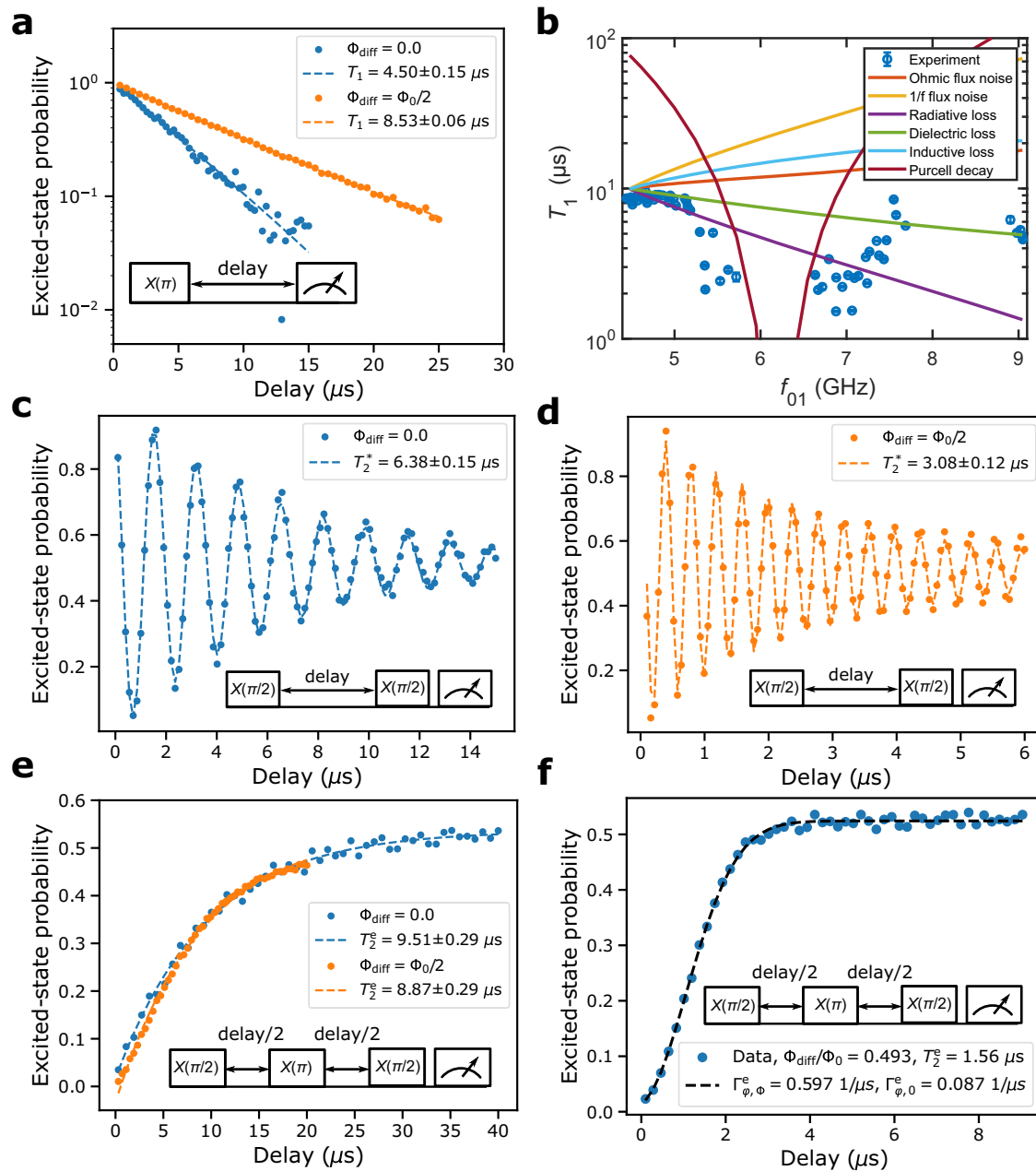


Fig. 8 | Energy relaxation and coherence for qubit B. **a** Excited-state probability as a function of the delay time between the state preparation and readout (see inset) at flux biases $\Phi_{\text{diff}} = 0$ (blue color) and $\Phi_{\text{diff}} = \Phi_0/2$ (orange color). The exponential fits (dashed lines) yield energy relaxation times $T_1 = 4.5 \pm 0.2 \mu\text{s}$ and $T_1 = 8.5 \pm 0.1 \mu\text{s}$ at $\Phi_{\text{diff}} = 0$ and $\Phi_0/2$, respectively. **b** Measured mean T_1 as a function of the qubit frequency f_{01} (blue circles) and its theoretical predictions from different indicated loss mechanisms that are scaled to coincide with the experimental data at $\Phi_{\text{diff}} = \Phi_0/2$ excluding Purcell decay. The error bars provide the standard error of the mean based on 6–30 repeated T_1 measurements. **c** Measured (markers) and fitted (dashed line) excited-state probability as a function of the delay time

between the $X(\pi/2)$ pulses of a Ramsey measurement (see inset) conducted at $\Phi_{\text{diff}} = 0$ using a detuning of 0.6 MHz between the drive and qubit frequencies. **d** As **c** but for $\Phi_{\text{diff}} = \Phi_0/2$ and a detuning of 2.5 MHz. **e** Measured excited-state probability (markers) as a function of the delay time between the $X(\pi/2)$ pulses in a T_2 echo measurement (see inset) conducted at the sweet spots $\Phi_{\text{diff}} = 0$ (blue color) and $\Phi_{\text{diff}} = \Phi_0/2$ (orange color). The dash lines provide exponential fits to the data. **f** As **e** but for $\Phi_{\text{diff}}/\Phi_0 = 0.493$. Here, the dashed line shows a model corresponding to a product of a Gaussian and an exponential with decay rates $\Gamma_{\varphi, \Phi}^e = 0.60 \mu\text{s}^{-1}$ and $\Gamma_{\varphi, 0}^e = 0.09 \mu\text{s}^{-1}$, respectively.

At $\Phi_{\text{diff}} = 0$ in contrast, we measure a Ramsey coherence time of $T_2^* = 6.8 \mu\text{s}$ and a T_1 -limited echo coherence time of $T_2^e = 9.9 \mu\text{s}$. The dephasing rate is lower here than at $\Phi_{\text{diff}} = -\Phi_0/2$ since the qubit frequency is less sensitive to the external flux difference due to the lower second-order contribution $|\partial^2 \omega_{01} / \partial^2 \Phi_{\text{diff}}|$. Note that the anharmonicity of the qubit at $\Phi_{\text{diff}} = 0$ is only $\alpha/(2\pi) = -58$ MHz, and hence this operation point is not of great interest for implementations of high-fidelity quantum logic.

Next, we demonstrate that the high anharmonicity of the unimon and its protection against charge and flux noise enable us to implement fast high-fidelity single-qubit gates. To this end, we calibrate single-qubit gates of duration $t_g \in [13.3, 46.6]$ ns using microwave pulses parametrized according to the derivative removal by adiabatic gate (DRAG) framework^{56,57}. To characterize the average fidelity of gates in the set $\{|, X(\pi/2), Y(\pi/2)\}$, we utilize interleaved randomized benchmarking⁵⁸ (“Methods”). Figure 4a shows that we reach a

practically coherence-limited fidelity of 99.9% for I , $X(\pi/2)$, and $Y(\pi/2)$ gates at 13.3 ns duration. Our electronics limit the shortest gate pulses to 13.3 ns although the anharmonicity should allow for high-fidelity gates down to 5 ns duration corresponding to a gate fidelity of 99.97% with the reported coherence properties.

To study the long-term stability of the gate fidelity, we first calibrate 20 ns single-qubit gates and then conduct repetitive measurements of the average gate fidelity using standard randomized benchmarking^{59,60} without any recalibration between repetitions. Figure 4b indicates that the measured gate fidelity is stable over the full period of eight hours with an average fidelity of $99.88 \pm 0.02\%$, practically coinciding with the coherence limit of 99.89%. This stability can be attributed to the relaxation time T_1 and the coherence times T_2^* and T_2^e staying practically constant in time as illustrated in Fig. 4c.

Discussion

In conclusion, we introduced and demonstrated the unimon qubit that has a relatively high anharmonicity while requiring only a single Josephson junction without any superinductors, and bearing protection against both low-frequency charge noise and flux noise. The geometric inductance of the unimon has the potential for higher predictability and reproducibility than the junction-array-based superinductors in conventional fluxoniums or in quartons. Thus, the unimon constitutes a promising candidate for achieving single-qubit gate fidelities beyond 99.99% in superconducting qubits with the help of the following future improvements: (i) redesign of the geometry to minimize dielectric losses⁶¹ currently dominating the energy relaxation, (ii) use of recently found low-loss materials²⁶, and (iii) reduction of the gate duration to values well below 10 ns allowed even by the anharmonicities achieved here. Future unimon research is also needed to study and minimize the various on-chip cross talks, implement two-qubit gates, and to scale up to many-qubit processors. To further reduce the sensitivity of the unimon to flux noise and to scale up the qubit count, it is likely beneficial to reduce the footprint of a single unimon qubit using, e.g., a superconductor with a high kinetic inductance in the coplanar-waveguide resonator. The anharmonicity of the unimon at flux bias $\Phi_{\text{diff}} = \Phi_0/2$ has an opposite sign to that of the transmon, which may be helpful to suppress the unwanted residual ZZ interaction with two-qubit-gate schemes that utilize qubits with opposite-sign anharmonicities^{62,63}. In analogy to the quarton, the dominance of the quartic term in the potential energy of the unimon may enable extremely fast two-qubit gates and qubit readout in schemes utilizing the unimon as a coupler for transmon qubits⁶⁴. The distributed-element nature of the unimon provides further opportunities for implementing a high connectivity and distant couplings in multi-qubit processors. The parameter values we have demonstrated in this work for the qubit-resonator coupling capacitance and for the corresponding coupling strength are sufficient for implementing high-fidelity two-qubit gates employing the typical coupling schemes for transmons^{65,66}, as we numerically simulate in Supplementary Note I in Supplementary Materials for the cross-resonance gate. In the future, we also aim to study the utilization of other modes of the unimon circuit, for example, for additional qubits and qubit readout.

Methods

Hamiltonian based on a model of coupled normal modes (model 1)

Here, we provide a brief summary of the theoretical model 1 that is used to derive a Hamiltonian for the unimon qubit, starting from the normal modes of the distributed-element circuit illustrated in Fig. 1c. A complete derivation is provided in Supplementary Methods I. In this theoretical model, we extend the approach of ref. 67 to model phase-biased Josephson junctions in distributed-element resonators in the presence of an external magnetic flux.

In the discretized circuit of Fig. 1c, the Josephson junction is located at x_j and we model the CPW resonator of length $2l$ using N inductances $L_l \Delta x$ and N capacitances $C_l \Delta x$ with $\Delta x = 2l/N$. Based on this circuit model, we construct the classical Lagrangian of the system using the node fluxes $\Psi_i = \int_{-\infty}^t V_i(t') dt'$ as the coordinates with V_i denoting the voltage across the i :th capacitor⁶⁸. From the Lagrangian, we derive the classical equations of motion for the node fluxes and take the continuum limit resulting in a continuous node-flux function $\psi(x) = \int_{-\infty}^t V(x, t') dt'$. Under the assumption of a sufficiently homogeneous magnetic field, the flux at the center conductor $\psi(x)$ is described with the wave equation $\psi = v_p^2 \partial_{xx} \psi$, where the phase velocity is given by $v_p = 1/\sqrt{L_l C_l}$, where L_l and C_l denote the inductance and capacitance per unit length. Furthermore, we obtain a set of boundary conditions corresponding to the grounding of the CPW at its end points and the current continuity across the junction.

In the regime of small oscillations about a minimum of the potential energy, the classical flux $\psi(x)$ can be decomposed into a sum of a dc component and oscillating normal modes. Using this decomposition and linearizing the junction in the vicinity of the dc operation point, we derive the classical normal-mode frequencies $\{\omega_m/(2\pi)\}_{m=0}^{\infty}$ and dimensionless flux-envelope functions $\{u_m(x)\}_{m=0}^{\infty}$. Subsequently, we invoke a single-mode approximation, in which the flux $\psi(x)$ is expressed as $\psi(x, t) = \Phi_0 \varphi_0 u_0(x)/(2\pi) + \psi_m(t) u_m(x)$, where m is the mode index corresponding to the qubit, φ_0 is the dc Josephson phase, and $\psi_m(t)$ describes the temporal evolution of the flux for the qubit mode m . The dc phase φ_0 is controlled by the flux bias Φ_{diff} as $\varphi_0 + 2lL_l \sin(\varphi_0)/L_j = 2\pi\Phi_{\text{diff}}/\Phi_0$, where $L_j = \Phi_0^2/(2\pi)^2/E_j$ is the effective Josephson inductance.

Finally, we quantize the classical Hamiltonian under the single-mode approximation and obtain

$$\hat{H}_m = 4E_{C,m}(\varphi_0)\hat{n}_m^2 + \frac{1}{2}E_{L,m}(\varphi_0)\hat{\varphi}_m^2 + E_L\hat{\varphi}_m\left(\frac{2\pi\Phi_{\text{diff}}}{\Phi_0} - \varphi_0\right) - E_J \cos(\hat{\varphi}_m - \varphi_0), \quad (4)$$

where \hat{n}_m and $\hat{\varphi}_m$ are the charge and phase operators corresponding to the qubit mode and satisfying $[\hat{\varphi}_m, \hat{n}_m] = i$, $E_L = \Phi_0^2/(2\pi)^2/(2lL_l)$ is the inductive energy of the dc component, and the capacitive energy $E_{C,m}(\varphi_0)$ and the inductive energy $E_{L,m}(\varphi_0)$ of the qubit mode m are functions of Φ_{diff} and circuit parameters according to Supplementary Eqs. (27), (30–34), (37–38), and (40) in Supplementary Methods I.

The phase-basis wave functions and the potential energy based on the Hamiltonian in Eq. (4) are illustrated in Fig. 5a, b for the parameter values of the qubit B. In Fig. 5c–e, we further show the characteristic energy scales of the unimon ($E_{C,m}, E_{L,m}, E_L$), the charge matrix elements $\langle i|\hat{n}_m|j\rangle$ and the phase matrix elements $\langle i|\hat{\varphi}_m|j\rangle$ as functions of Φ_{diff} , where we denote the k -photon state of mode m by $|k\rangle$.

In our qubit samples, each unimon is coupled to a readout resonator via a capacitance C_g at a location x_g to allow measurements of the qubit state. As derived in Supplementary Methods II, the Hamiltonian of the coupled resonator-unimon system is given by

$$\hat{H} = \hbar\omega_r\hat{a}_r^\dagger\hat{a}_r + \sum_j \hbar\omega_j|j\rangle\langle j| + \hbar \sum_{ij} \left(g_{ij}|i\rangle\langle j|\hat{a}_r^\dagger + g_{ij}^*|j\rangle\langle i|\hat{a}_r \right), \quad (5)$$

where $f_r = \omega_r/(2\pi)$ is the resonator frequency, \hat{a}_r is the annihilation operator of the readout resonator, $\{\hbar\omega_j\}$ and $\{|j\rangle\}$ are the eigenenergies and eigenstates of the bare unimon qubit, and the coupling strengths g_{ij} are given by

$$g_{ij} \approx 4\omega_r \frac{C_g u_m(x_g) \Delta u_m}{2C_l l + C_j + C_g u_m(x_g)^2} \sqrt{\frac{Z_{\text{tr}}}{R_K}} \langle i|\hat{n}_m|j\rangle, \quad (6)$$

where $\Delta u_m = u_m(x_g^+) - u_m(x_g^-)$, C_j is the junction capacitance, Z_{tr} is the characteristic impedance of the resonator, and $R_K = h/e^2$ is the von

Klitzing constant. Assuming that $|\omega_1 - \omega_0 - \omega_r| \gg |g_{01}|$, we invoke the dispersive approximation allowing us to simplify Eq. (5) as (see Supplementary Methods II)

$$\hat{H}_{\text{disp}} \approx \hbar \omega_r' \hat{a}_r^\dagger \hat{a}_r - \frac{\hbar \omega_{01}'}{2} \hat{\sigma}_z - \hbar \chi \hat{a}_r^\dagger \hat{a}_r \hat{\sigma}_z, \quad (7)$$

where ω_r' and ω_{01}' are the renormalized resonator and qubit frequencies, $\hat{\sigma}_z = |0\rangle\langle 0| - |1\rangle\langle 1|$, and the dispersive shift χ is approximately given by

$$\chi = \frac{|g_{01}|^2}{\omega_1 - \omega_0 - \omega_r} - \frac{1}{2} \frac{|g_{12}|^2}{\omega_2 - \omega_1 - \omega_r}. \quad (8)$$

Although the dispersive approximation involves a minor transformation of the qubit and resonator operators, we have for simplicity used identical symbols for the transformed and original operators.

Hamiltonian based on a path integral approach (model 2)

Here, we summarize our alternative theoretical approach for evaluation of the unimon spectrum. The unimon consists of a non-linear element (the Josephson junction) embedded into a linear non-dissipative environment (the $\lambda/2$ resonator) as shown in Fig. 1. This environment can be integrated out by the means of a path-integral formalism resulting in an effective action for a single variable, the flux difference ψ_- across the junction. This action appears to be both non-Gaussian and non-local in imaginary time, and hence extremely challenging to integrate it analytically. In order to obtain the low-frequency spectrum of the unimon, we approximate the non-local part of the action by coupling the ψ_- degree of freedom to M auxiliary linear modes, each described by a flux coordinate χ_k , $k = 1, \dots, M$. As described in detail in the Supplementary Methods I, the effective Hamiltonian of the unimon in this model reads as

$$\hat{H}_M = \frac{\hat{Q}^2}{2C} + \frac{\hat{\psi}_-^2}{2L_\psi} - E_J \cos \left[\frac{2\pi}{\Phi_0} (\hat{\psi}_- + \Phi_{\text{diff}}) \right] + \sum_{k=1}^M \left[\frac{\hat{q}_k^2}{2C} + \frac{C\chi_k^2}{2} \left(\frac{\pi k v_p}{2l} \right)^2 + \alpha_k \hat{\chi}_k \hat{\psi}_- \right], \quad (9)$$

where $[\hat{\chi}_k, \hat{q}_m] = i\hbar \delta_{km}$, $[\hat{\psi}_-, \hat{Q}] = i\hbar$, and all other single-operator commutators are zero, and the parameters C , L_ψ , and α_k are determined by Supplementary Eqs. (76)–(78). In the limit $M \rightarrow \infty$, this approximation becomes exact. We restrict our analysis to the lowest auxiliary mode which gives a non-vanishing contribution to the unimon spectrum. Note that if the unimon is symmetric ($x_j = 0$), the coupling of the Josephson junction to the first mode of the resonator vanishes, i.e., $\alpha_1 = 0$, and hence we need to consider the case $M = 2$. This approximation defines our model 2 which appears accurate enough for the quantitative analysis of the experimental data.

In addition to the technicalities related to the derivation of the models, the main difference between models 1 and 2 lies within the different employed approximations. In model 1, we take the linear part of the unimon into account exactly after linearizing the circuit at the minimum of the potential given by the dc phase, but we apply the single-mode approximation. Model 2 does not require us to solve the dc phase, and consequently we can conveniently work also in the regime $E_J > E_L$ which is problematic for model 1 owing to multiple solutions for the dc phase. The price we pay for this advantage is that we consider the linear part of the problem to some extent approximately and that we need to solve a multidimensional Schrödinger equation.

Design of the qubit samples

The samples are designed using QCCircuits⁶⁹ software which is built to work with the open-source computer-automated-design program KLayout⁷⁰. The designs are code-generated and parametrized for

convenient adjustments during the design process. As illustrated in Fig. 1e, each of the qubit chips comprise three unimon qubits which are capacitively coupled to individual readout resonators via U-shaped capacitors. All readout resonators are coupled with finger capacitors to the probe line using a single waveguide splitter. For multiplexed readout, the frequencies of the readout resonators are designed to be separated by 300 MHz. All of the unimons have the Josephson junction at the mid-point of the waveguide and are capacitively coupled to individual drive lines.

We present the design values of the main characteristic properties for all of the measured five qubits in Supplementary Table 2 in Supplementary Methods V. To obtain the geometries of the qubit circuits that yield the desired physical properties, first, the dimensions of the center conductor of the qubit are chosen in an effort to obtain the characteristic impedance of $Z = \sqrt{L_l/C_l} = 100 \Omega$. Here, the capacitance per unit length is $C_l = 2\epsilon_0(\epsilon_r - 1)r_1 + C_{\text{air}}$ and the inductance per unit length is $L_l = 1/(C_{\text{air}}c^2)$, where ϵ_0 is the vacuum electric permittivity, $\epsilon_r = 11.45$ is the relative dielectric constant of the substrate, $r_1 = K(r_2^2)/K(1 - r_2^2)$, where K denotes the complete elliptic integral of the first kind, $r_2 = \tanh[\pi a/(4\eta)]/\tanh[\pi b/(4\eta)]$, a is the width of the center conductor of the qubit, η is the thickness of the substrate, b is the total width of the qubit waveguide, $C_{\text{air}} = 2\epsilon_0(r_1 + r_3)$, where $r_3 = K(r_4^2)/K(1 - r_4^2)$, $r_4 = a/b$, and c is the speed of light⁷¹. Second, a series of finite-element simulations is executed on Ansys Q3D Extractor software to obtain the dimensions of the U-shaped capacitors with the target values of approximately 10 fF for the coupling capacitances C_g between the readout resonators and the qubits. Third, the dispersive shift of the qubit is approximated based on Eq. (8) as $\chi = \alpha |g_{01}|^2 / [\Delta(\Delta + \alpha)]$, where $\alpha/(2\pi) = 500$ MHz is a rough estimate for the anharmonicity of the unimon, $|g_{01}|/(2\pi)$ is the targeted coupling strength between the qubit and its readout resonator, and $\Delta = 2\pi(f_{01} - f_r)$. Finally, we adjust the length of the readout resonator and the capacitance C_k between the resonator and the probe line in order to obtain a resonator linewidth of $\kappa \approx \chi$ and a resonator frequency of f_r . To this end, we carry out the microwave modeling of the device netlist, from which we obtain estimates for the resonant modes and their respective linewidths.

Sample fabrication

The qubit devices were fabricated at the facilities of OtaNano Micro-nova cleanroom. First, we sputter a 200 nm-thick layer of highly pure Nb on a high-resistivity ($\rho > 10 \text{ k}\Omega\text{cm}$) non-oxidized undoped n -type (100) 6-inch silicon wafer. Then, the coplanar waveguide is defined in a mask aligner using photo resist. After development, the Nb film is etched with a reactive ion etching (RIE) system. After etching, the resist residuals are cleaned in ultrasonic bath with acetone and isopropyl alcohol (IPA), and dried with a nitrogen gun. Subsequently, the 6-inch wafer is cleaved into $3 \times 3 \text{ cm}^2$ dices by Disco DAD3220, including nine chips in total. Each chip is $1 \times 1 \text{ cm}^2$.

The tunnel junctions are patterned by a 100 keV EPBG5000pES electron beam lithography (EBL) system with a bilayer of methyl methacrylate/poly methyl methacrylate (MMA/PMMA) resist on a single chip. This is followed by a development in a solution of Methyl isobutyl ketone (MIBK) and IPA (1:3) for 20 s, Methyl Glycol for 20 s, and IPA for 20 s. The resist residues are cleaned with oxygen descum for 15 s. The two-angle shadow evaporation technique is applied to form the SIS junctions in an electron beam evaporator. Before evaporation, the native oxides are removed by Ar ion milling. Aluminum is deposited at a rate of 5 \AA/s . After lift off in acetone, each chip is cleaved by Disco DAD3220, then packaged and bonded with Al wires.

Measurement setup

For the experimental characterization, the packaged qubit devices are cooled down to a temperature of 10 mK using a commercial dilution refrigerator. The packaged samples are shielded by nested

mu-metal and Aluminum shields. The ports of the sample holder are connected to room temperature electronics according to the more detailed schematic diagram that can be found in Supplementary Methods IV.

To implement the microwave signals for driving the qubits, we up-convert in-phase (*I*) and quadrature-phase (*Q*) waveforms generated by an arbitrary waveform generator with the help of an *IQ* mixer and a local oscillator signal. The generated microwave signal is passed through a room temperature dc block and 60 dB of attenuation within the cryostat before reaching the sample.

For the qubit-state readout, we use an ultrahigh-frequency quantum analyzer (UHFQA) by Zurich Instruments. Using the UHFQA, we create an intermediate-frequency voltage signal that is up-converted to the frequency of the readout resonator with an *IQ* mixer and a local oscillator. The obtained microwave signal is passed through 60 dB of attenuation within the cryostat before entering the probe line. The output readout signal passes through two microwave isolators and a cryogenic high-electron-mobility transistor (HEMT) for amplification. At room temperature, the output signal is further amplified using a series of amplifiers and down-converted back to an intermediate frequency. In the UHFQA, the down-converted voltage signal is digitized and numerically converted to the base band. Due to the qubit-state-dependent dispersive shift of the readout resonator [see Eq. (7)], the measured output voltage is also dependent on the qubit state. To enable convenient calibration of the *IQ* mixer used for the qubit drive, the setup also includes a room temperature switch enabling us to alternatively down-convert and measure the up-converted drive signal.

To control the external flux difference, we use an external coil connected to a dc voltage source via two 50 k Ω resistors and a series of low-pass filters at room temperature and at the 100 mK stage of the cryostat. The coil is not specifically designed to yield a magnetic-field gradient required to bias the unimon, but such a gradient forms naturally owing to the simple circular shape of the coil and to the field-screening superconducting regions in the vicinity of the qubit. Note that the field does not need to be constant along the CPW structure although we have, for simplicity, invoked such an assumption in the derivation of model 1 in Supplementary Methods I.

Measurement and analysis of qubit frequency and anharmonicity

To measure the frequencies of the one-photon $|0\rangle \leftrightarrow |1\rangle$ transition and the two-photon $|0\rangle \leftrightarrow |2\rangle$ transition, we use a standard two-tone qubit spectroscopy experiment illustrated in Fig. 2c. In the experiment, we apply a continuous microwave signal to the drive line of the qubit while applying a readout signal through the probe line of the sample. At the sweet spot $\Phi_{\text{diff}} = \Phi_0/2$, we further measure the $|1\rangle \leftrightarrow |2\rangle$ transition frequency with an ef-Rabi experiment (see Fig. 6) in order to verify the anharmonicities shown in Fig. 3a and summarized in Table 1. In the ef-Rabi experiment, the qubit is first prepared to the excited state with a π -pulse followed by another pulse with a varying amplitude and a varying frequency around the estimated $|1\rangle \leftrightarrow |2\rangle$ transition. After the drive pulses, a readout pulse is applied and an oscillating output voltage is observed as a result of Rabi oscillations between the states $|1\rangle$ and $|2\rangle$.

To estimate the circuit parameters presented in Table 1, we use the following approach. First, we fit the theoretical Hamiltonian in Eq. (4) to the experimental transition frequencies of qubit B in order to estimate L_l , C_l , and E_j . Subsequently, the coupling capacitance C_g of qubit B is estimated by fitting Eq. (5) to the data of the avoided crossing in Fig. 2b. For the other qubits, it is assumed that L_l and C_l are equal to those of qubit B due to an identical geometry of the CPW. For these qubits, the Josephson energy E_j is first approximately fitted based on the measured $|0\rangle \leftrightarrow |1\rangle$ transition followed by an estimation of C_g using data of an avoided unimon-resonator crossing.

Characterization for readout

To characterize the device for qubit readout, we measure the dispersive shift $\chi/(2\pi)$ for all of the qubits. This is achieved using an experiment, in which the output readout signal is measured as a function of the signal frequency after preparing the qubit either to its ground or first excited state. In Fig. 7a, the measured dispersive shifts are compared against theoretical predictions computed with Eq. (8) based on the fitted circuit parameters, and the measured qubit frequency $\omega_{01}/(2\pi)$ and anharmonicity $\alpha/(2\pi)$. The good agreement between the experiment and the theory validates the dispersive approximation in Eq. (7).

We further measure the single-shot readout fidelity for qubit E with $\chi/(2\pi) = 4.1$ MHz. This is achieved by alternately preparing the qubit to the ground state and to the first excited state followed by a state measurement with a 1.6 μs -long readout pulse. The output readout voltage is obtained as an unweighted average of the voltage during a 1.6 μs -long integration window. This experiment is repeated 2000 times. Using an optimized threshold voltage, we extract a readout fidelity $[P(|0\rangle|0\rangle) + P(|1\rangle|1\rangle)]/2$ of 89.0% as shown in Fig. 7b, c. The readout error is dominated by qubit relaxation during the readout pulse. Note that the measured fidelity is reached without a quantum-limited amplifier suggesting that high-fidelity single-shot readout is possible with the unimon. Similarly, the relatively long readout time used in this work can be greatly shortened after the introduction of a quantum-limited amplifier.

Measurement and analysis of energy relaxation time

To measure the energy relaxation time T_1 , an initial π -pulse is applied to the ground-state-initialized qubit followed by a varying delay and a subsequent measurement of the qubit population. We use a single exponential function for fitting the qubit population, which is supported by the experimental data of qubit B shown in Fig. 8a. Thus, there is no evidence of quasiparticle-induced losses that result in a double-exponential decay.

For qubit B, the relaxation time is characterized across $\Phi_{\text{diff}}/\Phi_0 \in [0.0, 0.5]$ in order to determine the mechanisms limiting T_1 . As detailed in Supplementary Methods III, we model the relaxation rate $\Gamma_1 = 1/T_1$ due to a noise source λ as⁷²

$$\Gamma_1 = \frac{|\langle 0|\partial\hat{H}_m/\partial\lambda|1\rangle|^2}{\hbar^2} S_\lambda(\omega_{01}), \quad (10)$$

where $S_\lambda(\omega_{01})$ is the symmetrized noise spectral density of the variable λ at the qubit angular frequency ω_{01} . In Fig. 8b, we compare the frequency dependence of the measured relaxation rate to the theoretical models based on Ohmic flux noise, $1/f$ flux noise, dielectric losses, inductive losses, radiative losses, and Purcell decay through the resonator by scaling the theoretical predictions to coincide with the experimental data at $\Phi_{\text{diff}} = \Phi_0/2$. As illustrated in Fig. 3b, the experimental data is most accurately explained by a model including Purcell decay and dielectric losses with an effective dielectric quality factor of $Q_c = 3.5 \times 10^5$.

Measurement and analysis of coherence time

The coherence time of the qubits is characterized using standard Ramsey and Hahn echo measurements⁷³. At the sweet spots, we estimate the Ramsey coherence time T_2^* by fitting an exponentially decaying sinusoidal function to the measured qubit population, whereas we obtain the echo coherence time T_2^e using an exponential fit. As illustrated in Fig. 8c–e, these models agree well with the experimental data of qubit B at the flux-insensitive sweet spots yielding $T_2^* = 3.1 \mu\text{s}$ and $T_2^e = 8.9 \mu\text{s}$ for $\Phi_{\text{diff}} = \Phi_0/2$, and $T_2^* = 6.4 \mu\text{s}$ and $T_2^e = 9.5 \mu\text{s}$ for $\Phi_{\text{diff}} = 0$.

To study the sensitivity of the qubits to flux noise, we conduct Ramsey and Hahn echo measurements as a function of the external

flux bias in the vicinity of $\Phi_{\text{diff}} = \Phi_0/2$ (see Fig. 3c). In superconducting qubits, flux noise is often accurately described by $1/f$ noise^{74,75}

$$S_{\Phi_{\text{diff}}}(\omega) = \int_{-\infty}^{\infty} dt \exp(-i\omega t) \langle \Phi_{\text{diff}}(0) \Phi_{\text{diff}}(t) \rangle = 2\pi \frac{A_{\Phi_{\text{diff}}}^2}{\omega}, \quad (11)$$

where $A_{\Phi_{\text{diff}}}/\sqrt{\text{Hz}}$ is the flux noise density at 1 Hz. The $1/f$ -noise gives rise to a Gaussian decay in the echo experiment^{55,76}, due to which we model the Hahn echo decay with a product of Gaussian and exponential functions, $\propto \exp(-\Gamma_{\varphi,\Phi}^e t^2 - \Gamma_{\varphi,0}^e t)$, as illustrated in Fig. 8f. The corresponding T_2^e is evaluated as the $1/e$ decay time given by³⁹

$$T_2^e = \frac{\sqrt{4(\Gamma_{\varphi,\Phi}^e)^2 + (\Gamma_{\varphi,0}^e)^2} - \Gamma_{\varphi,0}^e}{2(\Gamma_{\varphi,\Phi}^e)^2}. \quad (12)$$

Under the assumption of $1/f$ -noise, the Gaussian dephasing rate $\Gamma_{\varphi,\Phi}^e$ obtained from an echo measurement is related to the flux noise density as^{55,76}

$$\Gamma_{\varphi,\Phi}^e = \sqrt{\ln 2} A_{\Phi_{\text{diff}}} \left| \frac{\partial \omega_{01}}{\partial \Phi_{\text{diff}}} \right| + \Gamma_{\varphi,x}^e, \quad (13)$$

where $\Gamma_{\varphi,x}^e$ is a small residual Gaussian decay rate at the sweet spot. For each of the qubits, we estimate the parameter $A_{\Phi_{\text{diff}}}$ in Table 2 by a linear least-squares fit to $(|\partial \omega_{01}/\partial \Phi_{\text{diff}}|, \Gamma_{\varphi,\Phi}^e)$ data, where $\partial \omega_{01}/\partial \Phi_{\text{diff}}$ is estimated by fitting a parabola $\omega_{01} = \tilde{a}\Phi_{\text{diff}}^2 + \tilde{b}\Phi_{\text{diff}} + \tilde{c}$ to the measured ω_{01} near the sweet spot and then evaluating $\partial \omega_{01}/\partial \Phi_{\text{diff}} = 2\tilde{a}\Phi_{\text{diff}} + \tilde{b}$.

For Ramsey experiments, we use an exponential decay model also away from the sweet spot to constrain the number of fitting parameters. The theoretical fit shown in Fig. 3c is based on a simple model of the form $1/T_2^* = a' |\partial \omega_{01}/\partial \Phi_{\text{diff}}| + b'$.

Implementation and benchmark of single-qubit gates

To implement fast high-fidelity single-qubit gates, we use the derivative removal by adiabatic gate (DRAG) framework⁵⁶. Thus, we parametrize the microwave pulses implementing the gates $V_{\text{rf}}(t) = I_{\text{qb}}(t) \cos(\omega_d t + \theta) + Q_{\text{qb}}(t) \sin(\omega_d t + \theta)$ as

$$I_{\text{qb}}(t) = A \exp\left[-\frac{(t - t_g/2)^2}{2\sigma^2}\right], t \in [0, t_g], \quad (14)$$

$$Q_{\text{qb}}(t) = \beta I'_{\text{qb}}(t), t \in [0, t_g], \quad (15)$$

where $\omega_d/(2\pi)$ is the drive frequency, θ determines the rotation axis of the gate, A and β are amplitudes of I_{qb} and Q_{qb} , respectively, t_g is the gate duration, and $\sigma = t_g/4$ is the standard deviation of the Gaussian. The drive frequency $\omega_d/(2\pi)$ is set to the qubit frequency $\omega_{01}/(2\pi)$ measured in a Ramsey experiment. The amplitude A of the Gaussian pulse is determined using error amplification by applying repeated π pulses with varying amplitudes A after an initial $\pi/2$ pulse. The amplitude β of the derivative component is chosen to minimize the difference of qubit populations measured after gate sequences $(X(\pi), Y(\pi/2))$ and $(Y(\pi), X(\pi/2))$ ⁷⁷.

To characterize the accuracy of the calibrated single-qubit gates, we use the definition of average gate fidelity⁷⁸. To measure the average gate fidelity, we use standard and interleaved randomized benchmarking (RB) protocols^{58–60}. In the standard RB protocol, we apply random sequences of Clifford gates appended with a final inverting gate and estimate the average fidelity of gates in the Clifford group F_{Cl} based on the decay rate of the ground state probability as a function of the sequence length. We decompose the Clifford gates based on Table 1 in ref. 79 using the native gate set $\{I, X(\pm\pi/2), Y(\pm\pi/2), X(\pi), Y(\pi)\}$

such that each Clifford gate contains on average 1.875 native gates. The average fidelity per a single native gate is estimated as $F_g = 1 - (1 - F_{\text{Cl}})/1.875$. To estimate the average gate fidelity of individual gates in the set $\{I, X(\pi/2), Y(\pi/2)\}$, we utilize the interleaved RB protocol, in which the average gate fidelity is measured by comparing the decay rates for sequences with and without the gate of interest interleaved after each random Clifford gate.

The theoretical coherence limit for the gate fidelity is computed based on the measured T_1 and T_2^e as $F_{g,\text{lim}} = 1/6 \times (3 + \exp(-t_g/T_1) + 2 \exp(-t_g/T_2^e))$ ³⁸.

Data availability

Data supporting the findings of this article is available at <https://doi.org/10.5281/zenodo.7052804>.

Code availability

The authors declare that the theoretical results used in the numerical algorithms for obtaining the findings of this study are available within the paper and its supplementary information.

References

- Arute, F. et al. Quantum supremacy using a programmable superconducting processor. *Nature* **574**, 505–510 (2019).
- Wu, Y. et al. Strong quantum computational advantage using a superconducting quantum processor. *Phys. Rev. Lett.* **127**, 180501 (2021).
- Yanay, Y., Braumüller, J., Gustavsson, S., Oliver, W. D. & Tahan, C. Two-dimensional hard-core Bose–Hubbard model with superconducting qubits. *npj Quantum Inform.* **6**, 1–12 (2020).
- Farhi, E., Goldstone, J. & Gutmann, S. A quantum approximate optimization algorithm. Preprint at <http://arxiv.org/abs/1411.4028> (2014).
- Dunjko, V. & Briegel, H. J. Machine learning & artificial intelligence in the quantum domain: A review of recent progress. *Rep. Prog. Phys.* **81**, 074001 (2018).
- McArdle, S., Endo, S., Aspuru-Guzik, A., Benjamin, S. C. & Yuan, X. Quantum computational chemistry. *Rev. Mod. Phys.* **92**, 015003 (2020).
- Preskill, J. Quantum computing in the NISQ era and beyond. *Quantum* **2**, 79 (2018).
- Nakahara, M. *Quantum Computing: From Linear Algebra to Physical Realizations* (CRC Press, 2008).
- Temme, K., Bravyi, S. & Gambetta, J. M. Error mitigation for short-depth quantum circuits. *Phys. Rev. Lett.* **119**, 180509 (2017).
- Kandala, A. et al. Error mitigation extends the computational reach of a noisy quantum processor. *Nature* **567**, 491–495 (2019).
- Gottesman, D. Stabilizer codes and quantum error correction. Ph.D. thesis, California Institute of Technology (1997).
- Fowler, A. G., Mariantoni, M., Martinis, J. M. & Cleland, A. N. Surface codes: Towards practical large-scale quantum computation. *Phys. Rev. A* **86**, 032324 (2012).
- Bonilla Ataides, J. P., Tuckett, D. K., Bartlett, S. D., Flammia, S. T. & Brown, B. J. The xzzx surface code. *Nat. Commun.* **12**, 1–12 (2021).
- Barends, R. et al. Superconducting quantum circuits at the surface code threshold for fault tolerance. *Nature* **508**, 500–503 (2014).
- Ofek, N. et al. Extending the lifetime of a quantum bit with error correction in superconducting circuits. *Nature* **536**, 441–445 (2016).
- Campagne-Ibarcq, P. et al. Quantum error correction of a qubit encoded in grid states of an oscillator. *Nature* **584**, 368–372 (2020).
- Andersen, C. K. et al. Repeated quantum error detection in a surface code. *Nat. Phys.* **16**, 875–880 (2020).
- Chen, Z. et al. Exponential suppression of bit or phase errors with cyclic error correction. *Nature* **595**, 383–387 (2021).

19. Marques, J. et al. Logical-qubit operations in an error-detecting surface code. *Nat. Phys.* **18**, 1–7 (2021).
20. Krinner, S. et al. Realizing repeated quantum error correction in a distance-three surface code. *Nature* **605**, 669–674 (2022).
21. Zhao, Y. et al. Realization of an error-correcting surface code with superconducting qubits. *Phys. Rev. Lett.* **129**, 030501 (2022).
22. Sundaresan, N. et al. Matching and maximum likelihood decoding of a multi-round subsystem quantum error correction experiment. Preprint at <http://arxiv.org/abs/2203.07205> (2022).
23. Acharya, R. et al. Suppressing quantum errors by scaling a surface code logical qubit. Preprint at <http://arxiv.org/abs/2207.06431> (2022).
24. Hertzberg, J. B. et al. Laser-annealing Josephson junctions for yielding scaled-up superconducting quantum processors. *npj Quantum Inform.* **7**, 1–8 (2021).
25. Zhu, Q. et al. Quantum computational advantage via 60-qubit 24-cycle random circuit sampling. *Sci. Bull.* **67**, 240–245 (2021).
26. Place, A. P. M. et al. New material platform for superconducting transmon qubits with coherence times exceeding 0.3 milliseconds. *Nat. Commun.* **12**, 1779 (2021).
27. Wang, C. et al. Towards practical quantum computers: Transmon qubit with a lifetime approaching 0.5 milliseconds. *npj Quantum Inform.* **8**, 1–6 (2022).
28. McKay, D. C., Wood, C. J., Sheldon, S., Chow, J. M. & Gambetta, J. M. Efficient z gates for quantum computing. *Phys. Rev. A* **96**, 022330 (2017).
29. Spring, P. A. et al. High coherence and low cross-talk in a tileable 3d integrated superconducting circuit architecture. *Sci. Adv.* **8**, eabl6698 (2022).
30. Sung, Y. et al. Realization of high-fidelity CZ and ZZ-free iSWAP gates with a tunable coupler. *Phys. Rev. X* **11**, 021058 (2021).
31. Marxer, F. et al. Long-distance transmon coupler with CZ gate fidelity above 99.8%. Preprint at <http://arxiv.org/abs/2208.09460> (2022).
32. Nakamura, Y., Pashkin, Y. A. & Tsai, J. S. Coherent control of macroscopic quantum states in a single-Cooper-pair box. *Nature* **398**, 786–788 (1999).
33. Koch, J. et al. Charge-insensitive qubit design derived from the Cooper pair box. *Phys. Rev. A* **76**, 042319 (2007).
34. Barends, R. et al. Coherent Josephson qubit suitable for scalable quantum integrated circuits. *Phys. Rev. Lett.* **111**, 080502 (2013).
35. Wood, C. J. & Gambetta, J. M. Quantification and characterization of leakage errors. *Phys. Rev. A* **97**, 032306 (2018).
36. Lescanne, R. et al. Escape of a driven quantum Josephson circuit into unconfined states. *Phys. Rev. Appl.* **11**, 014030 (2019).
37. Manucharyan, V. E., Koch, J., Glazman, L. I. & Devoret, M. H. Fluxonium: Single Cooper-pair circuit free of charge offsets. *Science* **326**, 113–116 (2009).
38. Bao, F. et al. Fluxonium: An alternative qubit platform for high-fidelity operations. *Phys. Rev. Lett.* **129**, 010502 (2022).
39. Zhang, H. et al. Universal fast-flux control of a coherent, low-frequency qubit. *Phys. Rev. X* **11**, 011010 (2021).
40. Somoroff, A. et al. Millisecond coherence in a superconducting qubit. Preprint at <http://arxiv.org/abs/2103.08578> (2021).
41. Nguyen, L. B. et al. High-coherence fluxonium qubit. *Phys. Rev. X* **9**, 041041 (2019).
42. Grünhaupt, L. et al. Granular aluminium as a superconducting material for high-impedance quantum circuits. *Nat. Mater.* **18**, 816–819 (2019).
43. Hazard, T. et al. Nanowire superinductance fluxonium qubit. *Phys. Rev. Lett.* **122**, 010504 (2019).
44. Peruzzo, M. et al. Geometric superinductance qubits: Controlling phase delocalization across a single Josephson junction. *PRX Quantum* **2**, 040341 (2021).
45. Earnest, N. et al. Realization of a lambda-system with metastable states of a capacitively shunted fluxonium. *Phys. Rev. Lett.* **120**, 150504 (2018).
46. Liu, F.-M. et al. Quantum design for advanced qubits. Preprint at <https://arxiv.org/abs/2109.00994> (2021).
47. Yan, F. et al. Engineering framework for optimizing superconducting qubit designs. Preprint at <http://arxiv.org/abs/2006.04130> (2020).
48. Pechenezhskiy, I. V., Mencia, R. A., Nguyen, L. B., Lin, Y.-H. & Manucharyan, V. E. The superconducting quasicharge qubit. *Nature* **585**, 368–371 (2020).
49. Gyenis, A. et al. Experimental realization of a protected superconducting circuit derived from the 0- π qubit. *PRX Quantum* **2**, 010339 (2021).
50. Kalashnikov, K. et al. Bifluxon: Fluxon-parity-protected superconducting qubit. *PRX Quantum* **1**, 010307 (2020).
51. Smith, W., Kou, A., Xiao, X., Vool, U. & Devoret, M. Superconducting circuit protected by two-cooper-pair tunneling. *npj Quantum Inform.* **6**, 1–9 (2020).
52. Blais, A., Huang, R.-S., Wallraff, A., Girvin, S. M. & Schoelkopf, R. J. Cavity quantum electrodynamics for superconducting electrical circuits: An architecture for quantum computation. *Phys. Rev. A* **69**, 062320 (2004).
53. Siddiqi, I. et al. Dispersive measurements of superconducting qubit coherence with a fast latching readout. *Phys. Rev. B* **73**, 054510 (2006).
54. Peruzzo, M., Trioni, A., Hassani, F., Zemlicka, M. & Fink, J. M. Surpassing the resistance quantum with a geometric superinductor. *Phys. Rev. Appl.* **14**, 044055 (2020).
55. Braumüller, J. et al. Characterizing and optimizing qubit coherence based on squid geometry. *Phys. Rev. Appl.* **13**, 054079 (2020).
56. Motzoi, F., Gambetta, J. M., Reberstrost, P. & Wilhelm, F. K. Simple pulses for elimination of leakage in weakly nonlinear qubits. *Phys. Rev. Lett.* **103**, 110501 (2009).
57. Chow, J. M. et al. Optimized driving of superconducting artificial atoms for improved single-qubit gates. *Phys. Rev. A* **82**, 040305 (2010).
58. Magesan, E. et al. Efficient measurement of quantum gate error by interleaved randomized benchmarking. *Phys. Rev. Lett.* **109**, 080505 (2012).
59. Magesan, E., Gambetta, J. M. & Emerson, J. Scalable and robust randomized benchmarking of quantum processes. *Phys. Rev. Lett.* **106**, 180504 (2011).
60. Magesan, E., Gambetta, J. M. & Emerson, J. Characterizing quantum gates via randomized benchmarking. *Phys. Rev. A* **85**, 042311 (2012).
61. Lahtinen, V. & Möttönen, M. Effects of device geometry and material properties on dielectric losses in superconducting coplanar-waveguide resonators. *J. Phys.: Condensed Matter* **32**, 405702 (2020).
62. Yan, F. et al. Tunable coupling scheme for implementing high-fidelity two-qubit gates. *Phys. Rev. Appl.* **10**, 054062 (2018).
63. Zhao, P. et al. High-contrast z-z interaction using superconducting qubits with opposite-sign anharmonicity. *Phys. Rev. Lett.* **125**, 200503 (2020).
64. Ye, Y., Peng, K., Naghiloo, M., Cunningham, G. & O'Brien, K. P. Engineering purely nonlinear coupling between superconducting qubits using a quarton. *Phys. Rev. Lett.* **127**, 050502 (2021).
65. Paroanu, G. S. Microwave-induced coupling of superconducting qubits. *Phys. Rev. B* **74**, 140504 (2006).
66. Rigetti, C. & Devoret, M. Fully microwave-tunable universal gates in superconducting qubits with linear couplings and fixed transition frequencies. *Phys. Rev. B* **81**, 134507 (2010).
67. Bourassa, J., Beaudoin, F., Gambetta, J. M. & Blais, A. Josephson-junction-embedded transmission-line resonators: From Kerr medium to in-line transmon. *Phys. Rev. A* **86**, 013814 (2012).

68. Vool, U. & Devoret, M. Introduction to quantum electromagnetic circuits. *Int. J. Circuit Theory Appl.* **45**, 897–934 (2017).
69. Heinsoo, J. et al. KQCCircuits <https://github.com/iqm-finland/KQCCircuits> (2021).
70. Köfferlein, M. KLayout <https://www.klayout.de/> (2021).
71. Simons, R. N. *Coplanar Waveguide Circuits, Components, and Systems* (John Wiley & Sons, 2004).
72. Schoelkopf, R., Clerk, A., Girvin, S., Lehnert, K. & Devoret, M. *Quantum Noise in Mesoscopic Physics* 175–203 (Springer, 2003).
73. Krantz, P. et al. A quantum engineer's guide to superconducting qubits. *Appl. Phys. Rev.* **6**, 021318 (2019).
74. Bylander, J. et al. Noise spectroscopy through dynamical decoupling with a superconducting flux qubit. *Nat. Phys.* **7**, 565–570 (2011).
75. Yan, F. et al. The flux qubit revisited to enhance coherence and reproducibility. *Nat. Commun.* **7**, 12964 (2016).
76. Ithier, G. et al. Decoherence in a superconducting quantum bit circuit. *Phys. Rev. B* **72**, 134519 (2005).
77. Reed, M. Entanglement and quantum error correction with superconducting qubits. Ph.D. thesis, Yale University (2013).
78. Nielsen, M. A. A simple formula for the average gate fidelity of a quantum dynamical operation. *Phys. Lett. A* **303**, 249–252 (2002).
79. Epstein, J. M., Cross, A. W., Magesan, E. & Gambetta, J. M. Investigating the limits of randomized benchmarking protocols. *Phys. Rev. A* **89**, 062321 (2014).
80. Peltonen, J. et al. Hybrid rf squid qubit based on high kinetic inductance. *Sci. Rep.* **8**, 1–8 (2018).
81. Hassani, F. et al. A superconducting qubit with noise-insensitive plasmon levels and decay-protected fluxon states. Preprint at <https://arxiv.org/abs/2202.13917> (2022).

Acknowledgements

S.K., A.G., O.K., V.V., and M.M. acknowledge funding from the European Research Council under Consolidator Grant No. 681311 (QUESS) and Advanced Grant No. 101053801 (ConceptQ), European Commission through H2020 program projects QMiCS (grant agreement 820505, Quantum Flagship), the Academy of Finland through its Centers of Excellence Program (project Nos. 312300, and 336810), and Business Finland through its Quantum Technologies Industrial grant No. 41419/31/2020. S.K. and M.M. acknowledge Research Impact Foundation for grant No. 173 (CONSTI). E.H. thanks Emil Aaltonen Foundation (grant No. 220056 K) and Nokia Foundation (grant No. 20230659) for funding. We acknowledge the provision of facilities and technical support by Aalto University at OtaNano - Micronova Nanofabrication Center and LTL infrastructure which is part of European Microkelvin Platform (EMP, No. 824109 EU Horizon 2020). We thank the whole staff at IQM and QCD Labs for their support. Especially, we acknowledge the help with the experimental setup from Roope Kokkonen, code and software support from Joni Ikonen, Tuukka Hiltunen, Shan Jolin, Miikka Koistinen, Jari Rosti, Vasiliy Sevriuk, and Natalia Vorobeva, and useful discussions with Brian Tarasinski.

Author contributions

The concept of the unimon qubit was conceived by E.H. and M.M. The theoretical model 1 was developed by E.H. with theory support from M.M., J.T., and J.Ha. The theoretical model 2 was developed by V.V. The qubit samples were designed by A.L., A.M., and C.O.-K. with support

from S.K. J.K., and D.J. had a significant role in developing the KQCCircuits software used for designing the unimon qubit devices. W.L. and T.L. designed Josephson Junctions. W.L. fabricated the qubit devices and benchmarked the room temperature resistance. M.P. helped on sample lift-off process. J. Ho. packaged the device. E.H. conducted the qubit measurements at IQM with support from F.M., C.F.C., and J.-L.O. regarding the experimental setup and from F.T., M.S., and K.J. regarding the measurement code. S.K. conducted the qubit measurements at QCD with support from A.G. E.H. analyzed the measurement data with support from S.K., V.V., and O.K. The manuscript was written by E.H. and M.M. with support from V.V., A.M., W.L., and S.K. All authors commented on the manuscript. Different aspects of the work were supervised by J.He., C.O.-K., T.L., J. Ha., and K.Y.T. M.M. supervised the work in all respects.

Competing interests

All authors except S.K., A.G., O.K., and V.V. declare that IQM Finland Oy has filed currently pending patent applications EP4012627A1, US20220190027A1, CN114626533A, and WO2022129693A1 and a granted utility model CN215895506U regarding the unimon qubit (operation principle, structure, and parameter regime) having the following inventors: Eric Hyyppä, Mikko Möttönen, Juha Hassel, and Jani Tuorila. S.K., A.G., O.K., and V.V. declare no competing interests.

Additional information

Supplementary information The online version contains supplementary material available at <https://doi.org/10.1038/s41467-022-34614-w>.

Correspondence and requests for materials should be addressed to Eric Hyyppä or Mikko Möttönen.

Peer review information *Nature Communications* thanks the anonymous reviewers for their contribution to the peer review of this work.

Reprints and permissions information is available at <http://www.nature.com/reprints>

Publisher's note Springer Nature remains neutral with regard to jurisdictional claims in published maps and institutional affiliations.

Open Access This article is licensed under a Creative Commons Attribution 4.0 International License, which permits use, sharing, adaptation, distribution and reproduction in any medium or format, as long as you give appropriate credit to the original author(s) and the source, provide a link to the Creative Commons license, and indicate if changes were made. The images or other third party material in this article are included in the article's Creative Commons license, unless indicated otherwise in a credit line to the material. If material is not included in the article's Creative Commons license and your intended use is not permitted by statutory regulation or exceeds the permitted use, you will need to obtain permission directly from the copyright holder. To view a copy of this license, visit <http://creativecommons.org/licenses/by/4.0/>.

© The Author(s) 2022